THE ASTROPHYSICAL JOURNAL, 442:381–400, 1995 March 20

THE TRANSITION REGIONS OF CAPELLA[1]

JEFFREY L. LINSKY,[2,3] BRIAN E. WOOD,[3] PHILIP JUDGE,[4] ALEXANDER BROWN,[3]
CATHERINE ANDRULIS,[3] AND THOMAS R. AYRES[5]

Received 1994 May 16; accepted 1994 September 29

ABSTRACT

We have used the Goddard High Resolution Spectrometer (GHRS) to observe the spectroscopic binary system Capella (G8 III + G1 III). Exposures with the G140L, G140M, G160M, G200M, and echelle gratings provide emission line profiles with unprecedented signal-to-noise and spectral resolving power ($\lambda/\Delta\lambda$) up to 92,000. Multi-Gaussian fits to the line profiles show that the hotter star contributes 60%–70% of the total flux in the chromospheric O I and Mg II resonance lines, but about 90% of the flux in the Si III, Si IV, and C IV lines formed in the transition region at $T \leq 10^5$ K. We find clear evidence that the emission lines from the hotter star are systematically redshifted relative to the photosphere with Doppler shifts of $+5 \pm 1$ km s^{-1} and $+9 \pm 3$ km s^{-1} in the chromospheric Mg II and O I lines, respectively, increasing to $+24 \pm 5$ km s^{-1} for the transition region Si IV 1393.8 Å line. The multi-Gaussian fits to permitted transition region lines of Si III, Si IV, C IV, and N V indicate the presence of three components: moderately broad lines formed in the transition region of the hotter star (component H), narrow lines formed in the transition region of the cooler star (component C), and very broad lines that we think are formed in microflares on the hotter star (component B). The He II 1640.4 Å feature has an broad profile, which indicates that it is formed by collisional excitation primarily from the hotter star, and a weak narrow component that we interpret as due to radiative recombination on the cooler star.

We observed spin-forbidden emission lines of C III], O III], Si III], O IV], O V], and S IV] that are sensitive to electron density. Fainter members of the O IV] multiplet and all of the S IV] lines have never before been seen in any star other than the Sun. We determine electron densities in the transition regions of the Capella stars using line ratios of O IV] lines and emission measure analysis. The emission measures are self-consistent only when the fluxes from each emitting component are considered separately. In particular, the transition region abundance distributions appear to be different on the two stars, and the spin-forbidden lines were not detected in the B component. The emission measures for component H (the G1 star) are consistent with a constant electron pressure (or hydrostatic equilibrium) transition region with $P_e = 10^{15+0.1}$ cm^{-3} K and possibly solar "coronal" abundances.

Subject headings: binaries: close — line: profiles — stars: coronae — stars: individual (α Aurigae) — ultraviolet: stars

1. INTRODUCTION

As the visually brightest of the spectroscopic binary systems, Capella (α Aur = HD 34029) often is chosen to test precise measurement techniques for determining orbital parameters, atmospheric parameters, evolutionary status of its component stars, and even the properties of the interstellar medium in its line of sight. Here we extend previous high-precision studies of Capella to the investigation of its chromosphere and transition region plasmas in the temperature range $3.7 \leq \log T_e \leq 5.3$. In particular, we exploit the high sensitivity, low instrumental noise, and low scattered light properties of the Goddard High-Resolution Spectrometer (GHRS) on the *Hubble Space Telescope*.

The most recent study of Capella's orbit and component parameters using the Mark III optical interferometer (Hummel et al. 1995) shows that the stars are in a circular orbit of 104.022 days period and 56.47 milliarcseconds semimajor axis. The visually fainter star (by $0^m.15$), called Aa, has a mass of $(2.69 \pm 0.06)\ M_\odot$, radius of $(12.2 \pm 0.2)\ R_\odot$, and spectral type G8 III (Strassmeier & Fekel 1990). The visually bright and hotter star, called Ab, has a mass of $(2.56 \pm 0.04)\ M_\odot$, radius of $(9.2 \pm 0.4)\ R_\odot$, and spectral type G1 III (Strassmeier & Fekel 1990). The assumption of coevolution allowed Hummel et al. to estimate the age of the system as 5.25×10^8 years and to infer that the more massive star has already undergone helium ignition. Despite their similar masses and radii, these stars have very different outer atmosphere layers, presumably due to the fast rotation ($v \sin i = 36$ km s^{-1}) of the hotter component but slow rotation ($v \sin i = 3$ km s^{-1}) of the cooler component (Ayres & Linsky 1980; Strassmeier & Fekel 1990).

Much has been learned about the chromospheres and transition regions of the Capella stars from the analysis of *IUE* spectra obtained at different oribital phases. As described below, Ayres & Linsky (1980) and Ayres (1984, 1988) have shown that the hotter star dominates the ultraviolet emission

[1] Based on observations with the NASA/ESA *Hubble Space Telescope*, obtained at the Space Telescope Science Institute which is operated by the Association of Universities for Research in Astronomy, Inc., under NASA Contract NAS5-26555.

[2] Staff Member, Quantum Physics Division, National Institute of Standards and Technology; jlinsky@jila.colorado.edu.

[3] Joint Institute for Laboratory Astrophysics, University of Colorado and National Institute of Standards and Technology, Boulder, CO 80309-0440, wood@jila.colorado.edu; ab@jila.colorado.edu; andulis@jila. colorado.edu.

[4] High Altitude Observatory, National Center for Atmospheric Research, Boulder, CO 80307-3000; judge@hao.ucar.edu.

[5] Center for Astrophysics and Space Astronomy, University of Colorado, Boulder, CO 80309-0391; ayres@vulcan.colorado.edu.

line spectrum of the system, and each star produces bright emission lines formed in solar-like chromospheres and transition regions. The composite X-ray spectrum appears to contain major contributions from coronal plasma at temperatures of 6 and 30 million degrees K (Swank et al. 1981). Capella also is a weak thermal radio source (Drake & Linsky 1986). In this paper we use the high quality GHRS spectra to identify three distinct components of the Capella transition region emission and to determine the location and physical properties of each. In a subsequent paper we will construct detailed models for each component.

2. OBSERVATIONS

We observed Capella on 1991 April 15 using the low, moderate, and high resolution gratings of the Goddard High Resolution Spectrometer (GHRS). For a description of the GHRS instrument see Brandt et al. (1992), and for a discussion of an orbit performance see Wahlgren et al. (1991) and Heap et al. (1995). Our observations were made near quadrature at orbital phase 0.26 ($\phi = 0.26$), with the G1 star moving at low velocity ($v_{rad} = +2.0$ km s^{-1}) and the G8 star moving away ($v_{rad} = +55.6$ km s^{-1}). Capella was observed again on 1993 September 19 near the opposite quadrature at $\phi = 0.80$ ($v_{rad} = +55.7$ km s^{-1} and $v_{rad} = +4.7$ km s^{-1} for the G1 and G8 stars, respectively). Orbital phases are based on the ephemeris in Batten, Fletcher, & Mann (1978), but with phase zero defined as the velocity crossing with the more massive star (G8) in front. Table 1 summarizes the observations.

With the exception of the one $\phi = 0.80$ G160M observation, all of the low and moderate resolution observations were obtained through the large science aperture (LSA) to maximize the throughput of the aberrated beam. The high dispersion echelle observations were taken through the small science aperture (SSA) to achieve the maximum possible spectral resolution for studies of the local interstellar medium, at the expense of decreased throughput. To obtain more accurate wavelength calibrations for the echelle spectra, spectral calibration lamp images were taken of the wavelength region of interest before the star was observed, with the exception of the $\phi = 0.80$ echelle spectra of Mg II. Wavelength calibration images also were taken for the $\phi = 0.26$ G200M observation of the 1880–1920 Å region and the $\phi = 0.80$ G160M observation of the 1205–1242 Å region. For a more complete description of the data reduction and the analysis of the $\phi = 0.26$ Capella echelle spectra, see Linsky et al. (1993a). The $\phi = 0.26$ and $\phi = 0.80$ spectra were processed with the 1992 June and 1993 December versions of the CALHRS calibration software, respectively (Duncan 1992). The GHRS detector uses an array of 500 diodes. The Capella observations were quarter-stepped, resulting in spectra with 2000 bins.

3. ANALYSIS OF THE LOW-DISPERSION SPECTRA

We obtained two low-dispersion spectra with the G140L grating in the broad spectral region 1161–1710 Å to measure the fluxes of important emission lines. Figure 1 shows that the ultraviolet spectrum of Capella is dominated by the resonance lines of H I, C II, Si III, Si IV, C IV, and N V which form at electron temperatures T_e of 20,000–150,000 K. Lyman-α is the brightest of the emission lines, despite strong interstellar hydrogen and deuterium absorption in its core which together extinguish nearly 60% of the intrinsic flux (Linsky et al. 1993a). Emission lines of other neutral species are weak, except for the O I multiplet near 1304 Å and the C I multiplet near 1657 Å. Table 2 lists the fluxes and observed wavelengths. Proposed identifications represent the species that we think dominate each distinct feature.

3.1. *The Resolution of the Low-Dispersion Spectra*

To determine the effective resolving power of the G140L grating with the LSA, given the blurred point spread function (PSF) of the telescope, we measured the full width at half maximum intensity (FWHM) of three strong unblended emission lines (Si III 1206 Å, Si IV 1394 Å, and He II 1640 Å). The mean FWHM is 1.58 Å, independent of wavelength. The empirical resolving power, $R = \lambda/\text{FWHM} = 830$ at 1305 Å and 990 at 1567 Å, is about half that measured through the SSA ($R = 2000$; see Ebbets 1992), as a result of the uncorrected spherical aberration of the *HST* primary mirror at the time of the observations.

TABLE 1

SUMMARY OF GHRS OBSERVATIONS

Grating	Aperture and Substep Pattern	Spectral Range (Å)	Spectral Resolution $\lambda/\Delta\lambda$	Spectral Resolution km s^{-1}	Exposure Time (s)	Start Time (UT)	Important Spectral Features
			$\phi = 0.26$				
G140L	LSA 5	1161–1449	830	360	27	07:05	H I, C II, Si IV
G140L	LSA 5	1425–1710	990	300	27	07:09	C IV, He II, O III]
G140M.....	LSA 5	1286–1313	15000	20	108	07:00	O I, S I, Si III
G160M.....	LSA 5	1384–1420	15000	20	377	05:38	Si IV, 0 IV], S IV]
G160M.....	LAS 5	1532–1567	15000	20	162	05:33	C IV, C I
G160M.....	LSA 5	1637–1672	15000	20	108	05:46	He II, C I, O III]
G200M.....	LSA 5	1730–1770	15000	20	27	05:31	N III]
G200M.....	LSA 5	1880–1920	15000	20	269	05:25	Si III], C III]
EA-46	SSA 9	1211–1217	84000	3.6	3878	10:04	H I, D I
EB-22	SSA 7	2594–2606	92000	3.3	700	13:37	Fe II
EB-20	SSA 7	2792–2807	85000	3.5	700	13:23	Mg II
			$\phi = 0.80$				
G160M.....	SSA 5	1205–1242	20000	15	1939	11:12	Si III, H I, O V], N V
EB-20	SSA 7	2792–2807	85000	3.5	700	12:50	Mg II

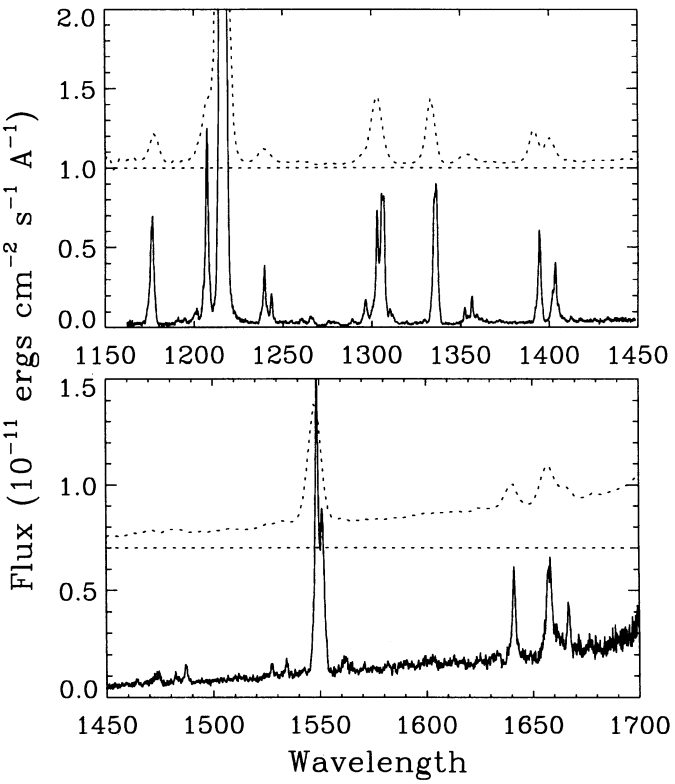

FIG. 1.—Two low-dispersion G140L spectra of Capella (*solid line*). The upper spectrum (*dotted line*) in both parts of the figure is a composite *IUE* spectrum obtained by coadding 31 SWP-LO spectra. The horizontal dotted lines indicate the zero flux levels for the displaced *IUE* spectrum.

3.2. *Comparison with IUE Low-dispersion Spectra of Capella*

Capella has been observed extensively by *IUE* (e.g., Ayres & Lindky 1980; Ayres 1984, 1988; Wood & Ayres 1995) to search for variability, to study line profiles, and to infer the relative contributions of each star to the composite spectrum. One important result is that Capella's emission line fluxes are remarkably steady with time and orbital phase. Ayres (1984, 1991), for example, could detect no significant photometric variations over orbital and rotational period timescales, and he concluded that the active G1 star of the Capella system, unlike the subgiants in shorter period RS CVn systems, must be covered nearly uniformly with active regions. Wood & Ayres (1995) and Ayres et al. (1995) have shown that Capella's emission line fluxes have not varied significantly over the decade and a half of the *IUE* mission.

The long term stability of the Capella UV spectrum permits intercomparison of the GHRS and *IUE* spectra obtained at different times to characterize the capabilities and limitations of each instrument. The two GHRS G140L spectra in Figure 1 each consist of one 27 s exposure. For comparison, we include a composite *IUE* spectrum obtained by coadding 31 SWP-LO spectra, 23 with about 10 minutes effective exposure time each, and eight of about 1 minute each (to provide a less overexposed Lyman-α line). The composite *IUE* spectrum includes both single and multiple offset exposures in the *IUE* LSA to minimize the fixed pattern noise of the *IUE* detector. The individual *IUE* spectra were photometrically corrected and extracted as described by Ayres et al. (1995). We believe that our composite low-dispersion spectrum of Capella represents the highest quality data achievable with *IUE*.

One striking difference between the two spectra is the 3 times higher spectral resolution of the GHRS (1.6 vs. 5 Å), which allows one accurately to identify and measure features that are blended in the *IUE* spectrum (see Table 2). For example, the weak feature near 1355 Å in the *IUE* spectrum is resolved by the GHRS into the Cl I 1352 Å, O I] 1356 Å, and O I] 1358 Å lines. In the *IUE* spectrum, the S I feature at 1296 Å is barely discernible as a blue wing excess in the strong O I line, but is cleanly separated by the GHRS.

In addition, the high dynamic range, low background, low scattered light level, and photon counting statistics of the GHRS permit us to measure the fluxes of faint lines that are not present or barely hinted in the composite *IUE* spectrum. Nevertheless, as shown in Figure 2 and Table 2, the integrated fluxes agree quite well for those features clearly visible in both the GHRS and *IUE* spectra. Indeed, the agreement is quite remarkable considering that the calibration of the new *IUE* reduction is completely independent of that of the GHRS and given the difficulty in determining precisely where the continuum lies, especially in the *IUE* spectrum.

4. ANALYSIS OF THE MODERATE DISPERSION LINE PROFILES

4.1. *Dissecting the Composite Capella Spectra*

Five of the six $\phi = 0.26$ moderate resolution spectra are displayed in Figure 3. The 1730–1770 Å spectral region is not

TABLE 2

LOW-DISPERSION EMISSION LINE FLUXES

Wavelength[a] (Å)	GHRS Flux (10^{-12} ergs cm^{-2} s^{-1})	*IUE* Flux (10^{-12} ergs cm^{-2} s^{-1})	Line ID
1176.1.....	17.0 ± 0.3	12.7 ± 0.5	C III
1190.9.....	0.8 ± 0.1	...	?
1194.3.....	1.4 ± 0.1	...	S III
1200.7.....	2.0 ± 0.1	...	S III
1207.1.....	23.7 ± 0.3	18.8 ± 0.5	Si III
1216.2.....	282 ± 1.0	290 ± 21	H I
1239.5.....	7.1 ± 0.1	8.8 ± 0.3	N V
1243.5.....	2.9 ± 0.1		N V
1260.7.....	0.4 ± 0.1	1.4 ± 0.3	Si II
1265.8.....	1.3 ± 0.1		Si II
1277.8.....	1.2 ± 0.1	...	C I?
1289.4.....	0.8 ± 0.1	...	C I
1296.4.....	3.3 ± 0.1	3.7 ± 0.1	S I
1302.8.....	12.5 ± 0.2	31.4 ± 0.3	O I
1306.0.....	22.0 ± 0.2		O I
1310.1.....	1.8 ± 0.1	...	Si II
1335.7.....	26.8 ± 0.2	23.7 ± 0.4	C II
1352.3.....	1.4 ± 0.1	4.1 ± 0.2	Cl I
1356.3.....	2.8 ± 0.1		O I]
1359.1.....	1.0 ± 0.1		O I]
1371.9.....	0.3 ± 0.1	...	O V
1394.3.....	12.3 ± 0.2	12.5 ± 0.5	Si IV
1403.3.....	10.0 ± 0.2	11.4 ± 0.5	Si IV
1412.5.....	0.4 ± 0.1	...	N I
1432.7.....	0.5 ± 0.1	...	C I
1473.6.....	1.8 ± 0.1	1.0 ± 0.1	S I
1482.7.....	0.8 ± 0.1	0.9 ± 0.1	S I?
1487.0.....	1.1 ± 0.1		N IV]
1527.3.....	0.7 ± 0.1	2.4 ± 0.6	Si II
1534.1.....	0.9 ± 0.1		Si II
1548.6.....	29.1 ± 0.3	41.0 ± 0.6	C IV
1551.4.....	15.5 ± 0.2		C IV
1561.5.....	1.3 ± 0.1	1.1 ± 0.2	C I
1641.0.....	7.5 ± 0.2	6.7 ± 0.4	He II
1657.4.....	12.5 ± 0.2	12.2 ± 0.2	C I
1666.7.....	3.5 ± 0.2	2.9 ± 0.2	O III]

[a] Observed wavelengths.

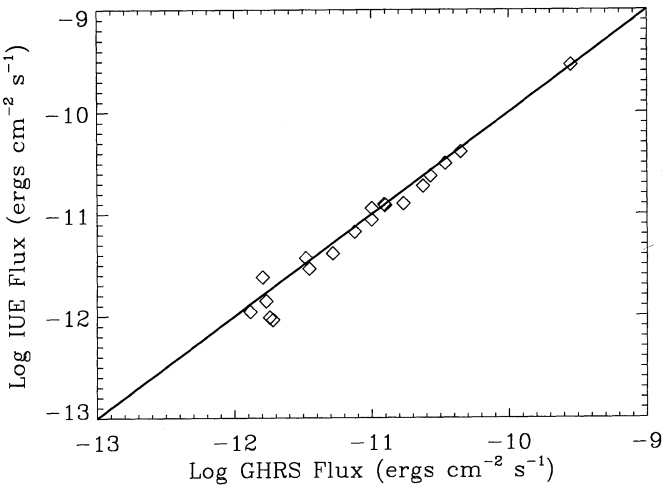

FIG. 2.—Comparison of emission line fluxes measured from the GHRS G140L spectra and the composite low-dispersion *IUE* spectrum of Capella. The solid line corresponds to equal GHRS and *IUE* line fluxes.

included because the spectrum is too noisy to reveal the N III] lines. Many of the individual lines from the $\phi = 0.26$ moderate resolution spectra are shown in Figure 4. Three key lines from the $\phi = 0.80$ G160M spectra are shown in Figure 5. (The Lyman-α line will be discussed in a future paper.) To estimate the velocities, widths, and fluxes of the lines, we first fitted each identified feature with a single Gaussian, except for the heavily

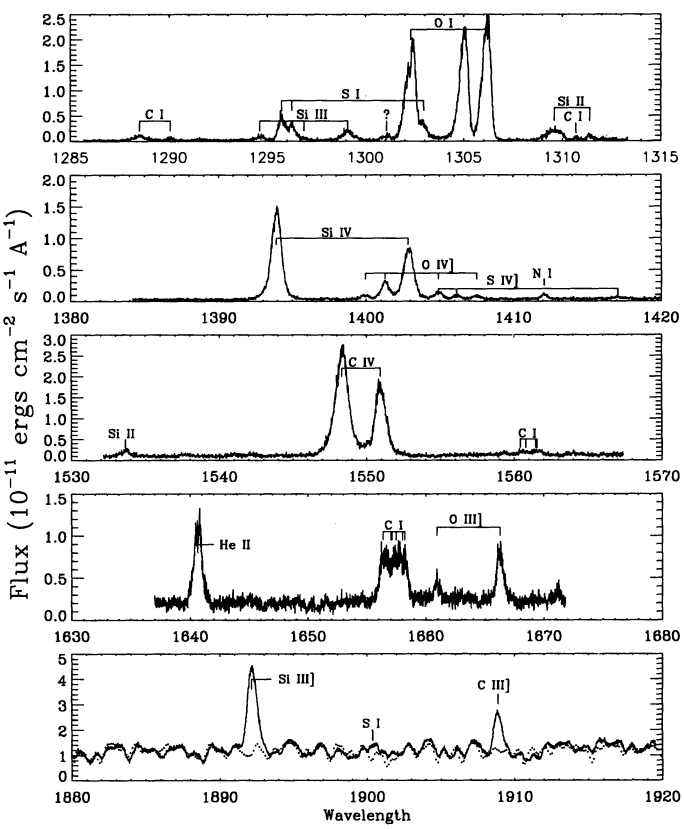

FIG. 3.—Five of the moderate resolution spectra, with line identifications. The dotted line shown in the 1880–1920 Å spectrum is a continuum predicted by a Kurucz model photosphere for Capella's G1 star.

blended C I multiplets at 1561 and 1657 Å. We subtracted the photospheric spectrum in the 1880–1920 Å region using a Kurucz model photosphere for the G1 star (shown as a dotted line in Fig. 3) before fitting the Si III] 1892.0 Å, S I 1900.3 Å, and C III] 1908.7 Å lines.

The results of the single-Gaussian fits are given in Table 3. The rest wavelengths are from Kelly (1987), except for O V] 1218.3 Å which is from Maran et al. (1994). The procedures outlined by Lenz & Ayres (1992) were used to estimate the 1 σ errors in the Gaussian parameters. For the features that lie on undulating continua, are blended with other lines, and/or are not well fit by a single Gaussian, we have arbitrarily tripled the errors computed from the prescription of Lenz & Ayres (1992). We could identify all of the prominent lines in the moderate resolution spectra except for the feature at 1301.075 Å, which has a FWHM of 0.566 Å and a total flux of 4.5×10^{-13} ergs cm^{-2} s^{-1}. It could be a blend of the S I 1300.900 Å and Si III 1301.149 Å lines, both of which are found in the solar spectrum (Sandlin et al. 1986).

Values of χ^2_ν were computed for the single-Gaussian fits (see Table 3) to determine if they were acceptable within a 2 σ criterion. The fits for the 12 strongest lines failed that test. We then attempted to fit these lines, except for Si III] 1892.0 Å and C III] 1908.7 Å, with two (or more) Gaussians. While our attempt to correct for the undulating continuum in the 1880–1920 Å region probably resulted in more accurate fluxes, widths, and wavelengths for the two intersystem lines, the LTE model continuum is not sufficiently reliable to compute believable multiple-Gaussian fits.

Figures 4 and 5 depict the results of the multi-Gaussian fits. Figure 5 also shows the single-Gaussian fit to the O V] 1218.4 Å line, which is superposed on the red wing of the Lyman-α line. The parameters for the multi-Gaussian fits are given in Table 4. For six of the 10 strong spectral lines, the total flux in all of the components listed in Table 4 lies within 1 σ of the flux obtained with the single-Gaussian fits, and for other four cases the agreement is within 2 σ. In fitting the lines observed at $\phi = 0.26$ through the LSA, we convolved the sum of the Gaussians with the instrumental profiles shown in Figure 6. Since the $\phi = 0.80$ spectrum was taken through the SSA, the use of convolved profiles was not necessary. The single-Gaussian fits of the lines observed at $\phi = 0.26$ were also performed using convolved profiles, although Capella's UV line profiles are too broad for the instrumental profile to affect significantly the results of these simple fits. When extracting more than one Gaussian component from a single profile, however, the subtle effects of the aberrated instrumental profile on the line shape should be taken into account, especially for narrow lines.

For all of the fits in Figure 4, the narrow solid lines illustrate the individual Gaussian components, while the thick solid line is the sum of the components convolved with the instrumental profile. The Gaussian components of the strong O I, Si IV, C IV, Si III, and N V lines in Figures 4 and 5 fall into five general categories: three emission types (see below) and two absorption types (central reversals and very narrow interstellar lines). (The He II 1640.4 Å line is discussed in § 4.4.) Dominating most of the fits is a moderately broad component that originates from the G1 star which dominates Capella's UV line emission (Ayres & Linsky 1980). We refer to that component as "H" (for hotter star). It is redshifted relative to the photosphere of the G1 star by about 9 ± 3 km s^{-1} for the O I lines and 16 ± 3 km s^{-1} for the transition region lines (Si III, N V,

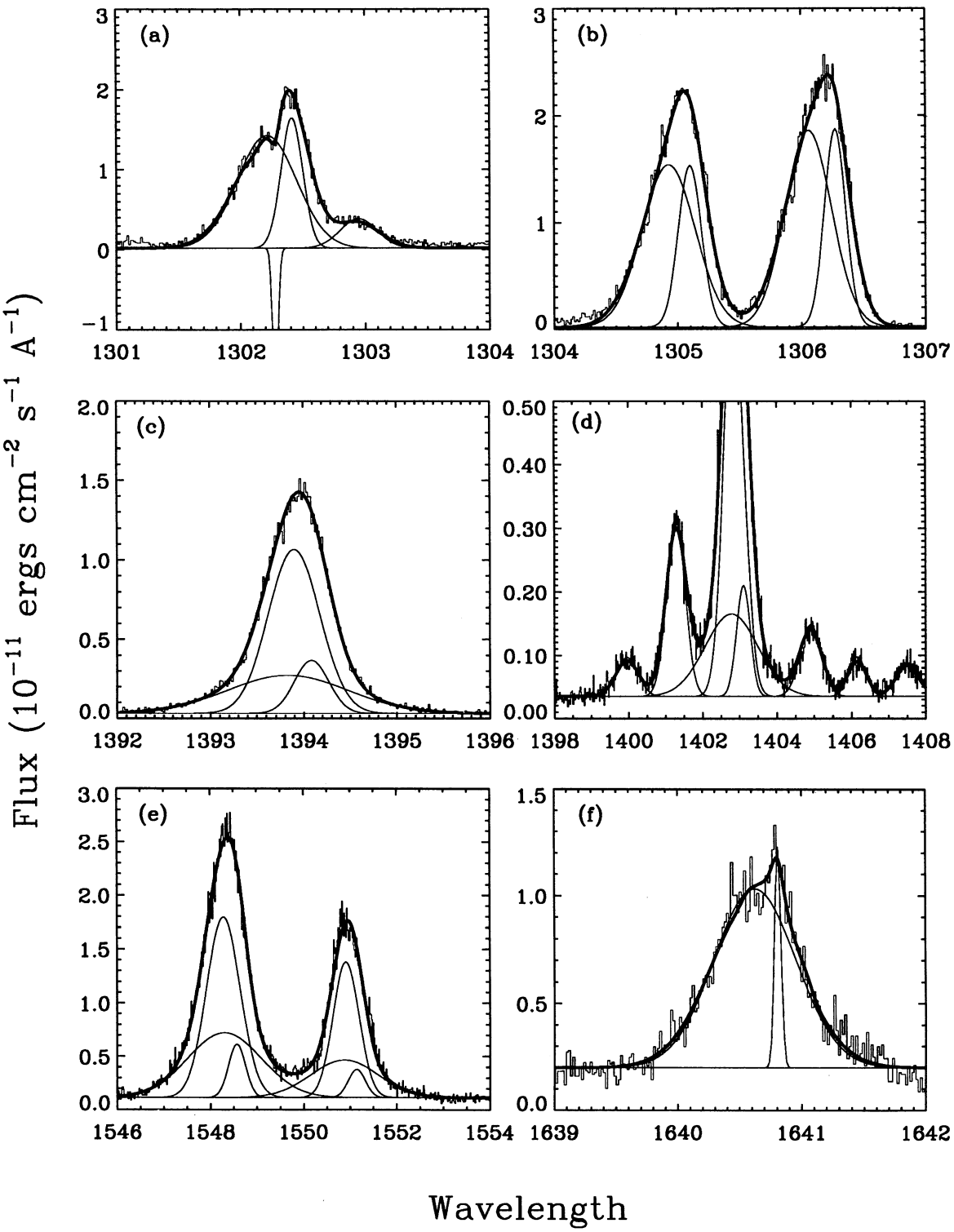

FIG. 4.—These are the multi-Gaussian fits that were performed on lines observed with the moderate resolution gratings at orbital phase 0.26. The observed line profiles are shown in histogram form. In all cases, the thin solid lines are the individual Gaussian components, and the thick solid line is the convolution of the sum of these components with the instrumental profile. See text for an explanation of the meaning of the components. The lines that have been fit are (*a*) the O I 1302.2 Å line and the S I 1302.9 Å line in its red wing; (*b*) the O I 1304.9 Å and O I 1306.0 Å lines; (*c*) the Si IV 1393.8 Å line; (*d*) the Si IV 1402.8 Å line along with the O IV] and S IV] lines (where the figure has been scaled to focus on these important O IV] and S IV] lines); (*e*) the C IV 1548.2 Å and C IV 1550.8 Å lines; and (*f*) the He II 1640.4 Å line.

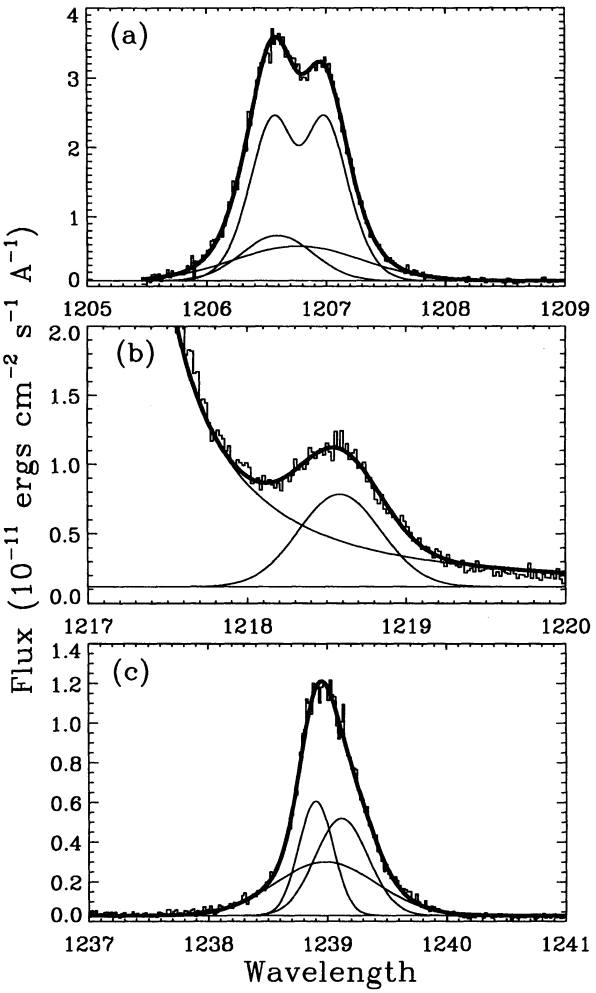

FIG. 5.—Fits to the three transition region lines observed at orbital phase 0.8. In all cases, the thin solid lines are the individual components of the fit, and the thick solid line is the sum of these components. Since the observation in which these lines were observed utilized the small science aperture rather than the large science aperture, the convolution step used in the fits shown in Fig. 4 was not necessary. The fitted lines are (*a*) the Si III 1206.5 Å line (which required an absorption Gaussian to model the observed central reversal, as well as three emission Gaussians); (*b*) the O V] 1218.3 Å line in the red wing of Lyman-α; and (*c*) the N V 1238.8 Å line.

Si IV, and C IV). (The uncertainties are the standard error of the mean rather than the standard deviation.) This is not unexpected because many stars, including Capella and the Sun, have redshifted chromospheric and transition region lines (Ayres, Jensen, & Engvold 1988; Hassler, Rottman, & Orrall 1991).

The permitted transition region lines all have very extended wing emission which suggested that a very broad Gaussian component should be included in the fits. We believe that this component, which we refer to as "B" (for very broad line), originates from the G1 star because the velocities are much closer to the radial velocity of the G1 star than to the G8 star.

For the lines listed in Table 4, we believe we have also detected emission from the G8 star. We refer to this third narrow component as "C" (for cooler star). The presence of the C component is obvious in the O I triplet; the three lines are noticably asymmetric due to the different central wavelengths and widths of the H and C components. Nevertheless, the two components are blended to the extent that many different combinations of components could be used to explain the profiles. We decided to constrain the fits by fixing the velocity of the C component to be the radial velocity of the G8 star. In particular, there is no evidence in the literature for significant line redshifts of O I in the spectra of late G giants. The other fit parameters were left unconstrained. The narrow interstellar absorption feature seen in the 1302.2 Å line, but not in the excited members of the multiplet, is discussed in § 4.5.

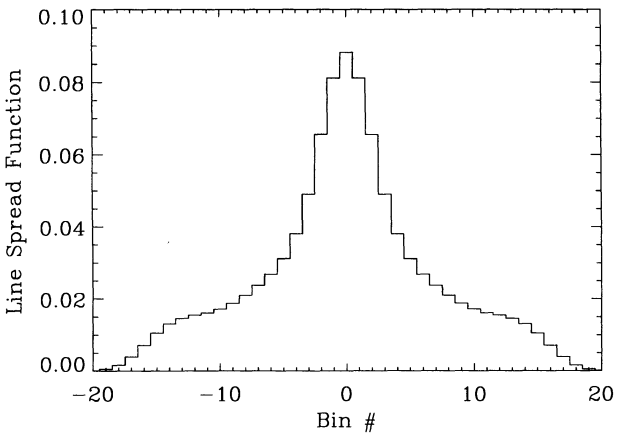

FIG. 6.—Instrumental profile for the GHRS, as produced by the PSF.CONSTRUCT program on the GHRS computer (Duncan 1992). The *X*-axis is in bin units. To find out the number of angstroms per bin for a given spectrum, divide the range of the spectrum in angstroms (given in Table 1) by 2000, since all of the spectra use 2000 bins.

After fitting the C IV 1548.2 Å line with two Gaussians, an H and a B component, we found the result was still not a 2 σ solution according to the χ^2 criterion. We interpreted the excess emission on the red side of the line as a detection of a C component and fitted the profile with three Gaussians. We again found it necessary to fix the position of the C component, but since transition region lines of late G giants *are* often found to have significant redshift (see β Ceti, for example, in Ayres et al. 1983), we assumed a typical redshift of 15 km s^{-1} for the C component of the transition region lines.

When the Si IV 1393.8 Å line was fitted with two Gaussians, an H and a B component, the result *was* a 2 σ solution. However, the presence of some excess emission on the red side of this line led us to include the C component as well. To obtain a reasonable three-Gaussian fit for this line, we had to fix the redshift of the C component to be 15 km s^{-1} and the width of the line to be the same as was found for the C component of the C IV 1548.2 Å line (0.43 Å). Figure 7*c* shows our best fit to the Si IV 1393.8 Å line and the residuals of the fit. Figures 7*a* and 7*b* illustrate how the quality of the fit decreases when the B and C components are removed. The importance of the B component is revealed by comparing Figure 7*a* with 7*c*. The reduced chi-squared drops from 3.61 to 1.06 when the B component is added. The presence of the C component is not as obvious from Figure 7. However, χ^2_ν is lower for the three-Gaussian fit, and the F test (e.g., Bevington & Robinson 1992) suggests that the quality of the three-Gaussian fit is sufficiently better than that of Figure 7*b* to warrant inclusion of the C component. Perhaps the strongest justification for the inclusion of the C component is that Ayres (1988) has convincingly shown—through ratios of *IUE* spectra obtained at opposite quadratures—that the G8 star accounts for roughly 10% of the flux in Capella's transition region lines.

We were not able to find any evidence for a C component in the Si IV 1402.8 Å and C IV 1550.8 Å line profiles. However, the

TABLE 3

LINE PROFILE ANALYSIS (SINGLE GAUSSIAN FITS)

Ion	λ_{rest} (Å)	λ_{meas} (Å)	v (km s^{-1})	f (10^{-13})	FWHM (Å)	χ^2_ν
Low-Excitation Permitted Lines						
C I	1288.422	1288.498	18 ± 4	5.9 ± 0.3	0.66 ± 0.03	0.988
C I	1289.977	1290.049	17 ± 4	1.3 ± 0.2	0.28 ± 0.03	1.259
C I	1310.637	1310.696	14 ± 2	0.9 ± 0.2	0.10 ± 0.02	1.310
C I	1561 mult	...	...	14.2 ± 0.4	...	...
C I	1657 mult	...	...	118 ± 2.0	...	...
N I	1411.949	1412.073	26 ± 2	3.2 ± 0.2	0.32 ± 0.01	1.061
S I	1295.653	1295.720	16 ± 1	18.1 ± 0.7	0.33 ± 0.01	1.142
S I	1296.174	1296.248	17 ± 2	12.7 ± 0.6	0.37 ± 0.01	1.142
S I	1302.863	1302.945	19 ± 1	13.6 ± 0.5	0.35 ± 0.01	1.225
S I	1900.286	1900.382	15 ± 1	32.1 ± 1.2	0.45 ± 0.02	2.720
Si II	1309.458	1309.596	32 ± 3	15.9 ± 0.7	0.78 ± 0.03	1.426
Si II	1311.265	1311.402	31 ± 3	2.5 ± 0.3	0.24 ± 0.02	1.317
Si II	1533.432	1533.624	38 ± 2	9.1 ± 0.4	0.65 ± 0.02	1.317
Weighted average[a]			19 ± 2			
Low-Excitation Optically Thick Lines						
O I	1302.169	1302.294	29 ± 3	112 ± 5	0.61 ± 0.02	3.541
O I	1304.858	1304.986	30 ± 2	115 ± 5	0.47 ± 0.02	4.249
O I	1306.029	1306.128	23 ± 2	122 ± 6	0.43 ± 0.02	5.497
Weighted average[a]			27 ± 2			
Optically Thin Transition Region Lines						
He II	1640.4 mult	1640.643	(30 ± 4)	75 ± 5	0.74 ± 0.03	1.565
C III]	1908.734	1908.869	21 ± 1	99 ± 2	0.53 ± 0.01	2.045
O III]	1660.803	1660.916	20 ± 2	9.7 ± 0.4	0.42 ± 0.02	1.084
O III]	1666.153	1666.271	21 ± 1	37 ± 1	0.59 ± 0.01	0.911
Si III	1294.543	1294.614	17 ± 4	2.8 ± 0.3	0.41 ± 0.03	1.293
Si III	1296.726	1296.857	30 ± 3	1.1 ± 0.2	0.21 ± 0.02	1.142
Si III	1298.960	1299.081	28 ± 3	11.3 ± 0.5	0.66 ± 0.02	1.038
Si III]	1892.030	1892.167	22 ± 1	263 ± 4	0.67 ± 0.01	3.747
O IV]	1399.774	1399.947	37 ± 3	4.3 ± 0.2	0.63 ± 0.02	1.078
O IV]	1401.156	1401.278	26 ± 1	17.3 ± 0.4	0.58 ± 0.01	1.032
O IV]	1407.386	1407.504	25 ± 3	3.8 ± 0.2	0.68 ± 0.02	0.908
O IV] + S IV]	1404.8bl	1404.902	(22 ± 2)	7.9 ± 0.3	0.66 ± 0.02	0.993
S IV]	1406.060	1406.148	19 ± 2	3.5 ± 0.2	0.53 ± 0.02	0.790
S IV]	1416.930	1417.658	27 ± 3	1.5 ± 0.1	0.57 ± 0.03	1.004
Weighted average[a]			23 ± 1			
Transition Region Resonance Lines						
C IV	1548.202	1548.321	23 ± 3	286 ± 8	1.19 ± 0.02	2.832
C IV	1550.774	1550.930	30 ± 3	159 ± 6	0.96 ± 0.03	2.305
Si IV	1393.755	1393.918	35 ± 2	121 ± 3	0.83 ± 0.02	5.038
Si IV	1402.770	1402.885	25 ± 3	69 ± 3	0.81 ± 0.02	2.101
Weighted average[a]			30 ± 3			
Lines Observed at Orbital Phase 0.80						
Si III	1206.510	1206.741	57 ± 2	324 ± 8	0.86 ± 0.02	5.220
N V	1238.821	1239.013	47 ± 2	75 ± 2	0.66 ± 0.02	3.737
O V]	1218.344	1218.583	59 ± 3	43 ± 2	0.61 ± 0.02	0.887
Weighted average[a]			51 ± 4			

[a] Errors cited are standard errors of the mean.

existence of C components in the stronger member of each doublet requires that C components be included in the weaker members. Thereafter, we fitted the Si IV 1402.8 Å and C IV 1550.8 Å lines with C components having the same redshift and width parameters as the C components in the Si IV 1393.8 Å and C IV 1548.2 Å lines, but with one-half the strengths (the optically thin limit for the doublets).

In the Si IV and C IV line profiles observed at $\phi = 0.26$, the G1 star's emission is on the blue side of the lines and the G8 star's emission is on the red side. The sense is reversed at $\phi = 0.80$. The Si III and N V lines we observed at the latter phase show more significant differences relative to the C IV and Si IV lines than the simple switching of the H and C components (see Fig. 5). While the two peaks seen in the Si III 1206.5 Å line could be caused by the sum of two emission components, the position of the red peak is too far to the red and too narrow to be explained by emission from the G1 star. We believe instead that the central dip in the Si III 1206.5 Å line

TABLE 4

LINE PROFILE ANALYSIS (MULTIPLE GAUSSIAN FITS)

Ion	λ_{rest} (Å)	λ_{meas} (Å)	v_{G1}[a] (km s^{-1})	f_{G1} (10^{-13})	FWHM$_{G1}$ (Å)	v_{G8}[b] (km s^{-1})	f_{G8} (10^{-13})	FWHM$_{G8}$ (Å)
O I	1302.169	1302.210	8	84	0.56			
O I	1302.169	1302.410				0	35	0.20
O I	1304.858	1304.928	14	82	0.50			
O I	1304.858	1305.099				0	36	0.22
O I	1306.029	1306.056	4	86	0.44			
O I	1306.029	1306.271				0	40	0.20
Flux-weighted average[c]			9 ± 3			0		
Si III	1206.510	1206.772	9	301	0.66			
Si III	1206.510	1206.772	9	−86	0.35			
Si III	1206.510	(1206.761)	(7)	(67)	(1.26)			
Si III	1206.510	1206.589				15	49	0.70
N V	1238.821	1239.118	16	27	0.53			
N V	1238.821	(1238.983)	(−17)	(29)	(1.00)			
N V	1238.821	1238.902				15	21	0.34
Si IV	1393.755	1393.899	29	72	0.65			
Si IV	1393.755	(1393.827)	(14)	(39)	(1.52)			
Si IV	1393.755	1394.083				15	15	0.43
Si IV	1402.770	1402.853	16	43	0.64			
Si IV	1402.770	(1402.776)	(−1)	(23)	(1.68)			
Si IV	1402.770	1403.100				15	8	0.43
C IV	1548.202	1548.280	13	152	0.85			
C IV	1548.202	(1548.300)	(17)	(119)	(1.85)			
C IV	1548.202	1548.566				15	23	0.43
C IV	1550.774	1550.910	24	89	0.66			
C IV	1550.774	(1550.872)	(17)	(64)	(1.71)			
C IV	1550.774	1551.139				15	12	0.43
Flux-weighted average[c]			16 ± 3			15		
Flux-weighted average[c]			(10 ± 4)					
He II	1640.438[d]	1640.623	32	69	0.78			
He II	1640.474[e]	1640.808				6	7	0.06
Mg II	2795.528	2795.603[f]	6	6440	1.34			
Mg II	2795.528	2795.603	6	−2550	0.75			
Mg II	2795.528	2796.096				5	3830	0.74
Mg II	2795.528	2796.096				5	−1370	0.39
Mg II	2802.705	2802.761	4	4790	1.26			
Mg II	2802.705	2802.761	4	−1850	0.70			
Mg II	2802.705	2803.249				3	2610	0.68
Mg II	2802.705	2803.249				3	−930	0.36
Flux-weighted average[c]			5 ± 1			4 ± 1		

[a] Velocity with respect to radial velocity of the G1 star (+2.0 km s^{-1} at $\phi = 0.26$ and +55.7 km s^{-1} at $\phi = 0.80$).
[b] Velocity with respect to radial velocity of the G8 star (+55.6 km s^{-1} at $\phi = 0.26$ and +4.7 km s^{-1} at $\phi = 0.80$).
[c] Errors cited are standard errors of the mean.
[d] Centroid laboratory wavelength for the collisional excitation model.
[e] Laboratory wavelength for the dominant line in the radiative recombination model.
[f] For Mg II, the measured wavelengths given are for the observation at orbital phase 0.26.

profile is due to a self reversal, indicating significant optical thickness at line center. We therefore fitted the H component of the line, as shown in Figure 5*a*, with two Gaussians (one in emission and the other in absorption) forced to have the same central wavelength. Our choice of Gaussians to represent the absorption and emission components is motivated mostly by expedience, although such profiles would be expected theoretically if Doppler broadening dominates in the line formation regions. Both a B and a C component have also been detected in this line. The C component is much broader than those detected in the C IV, Si IV, N V, and O I lines. Nevertheless, β Ceti (K0 III), which is thought to be similar to Capella's G8 star, also has a Si III 1206.5 Å line that is at least twice as broad as its other transition region lines (Ayres 1988). In fact, the width of β Ceti's Si III 1206.5 Å line is very close to that given in Table 4 for Capella's C component. The enhanced broadening undoubtedly is due to large optical depth.

With its asymmetric profile, the N V 1238.8 Å line has a shape like that of the chromospheric O I lines, suggesting that the G8 star is an important contributor. Our fit to the profile shows that the C component is much stronger than for the other transition region lines. In fact, our fits indicate that the C IV and N V fluxes from the G8 star are very similar, as previously was seen for β Ceti (Ayres et al. 1983).

With the notable exception of the Si III 1206.5 Å line, the H components are always much broader than the C components. The more rapid rotation of the G1 star ($v \sin i = 36$ km s^{-1}) compared to the G8 star ($v \sin i = 3$ km s^{-1}; Strassmeier & Fekel 1990) can play only a small role, since the FWHM is 230 ± 6 km s^{-1} for the C IV 1548.2 Å line and 185 ± 6 km s^{-1} for the 1550.8 Å line. These widths also are much larger than the predicted thermal width, $\Delta\lambda_D = 19.5$ km s^{-1}, and the instrumental width of 20 km s^{-1}, but are consistent with *IUE* observations at quadrature (Ayres 1984). We note that the

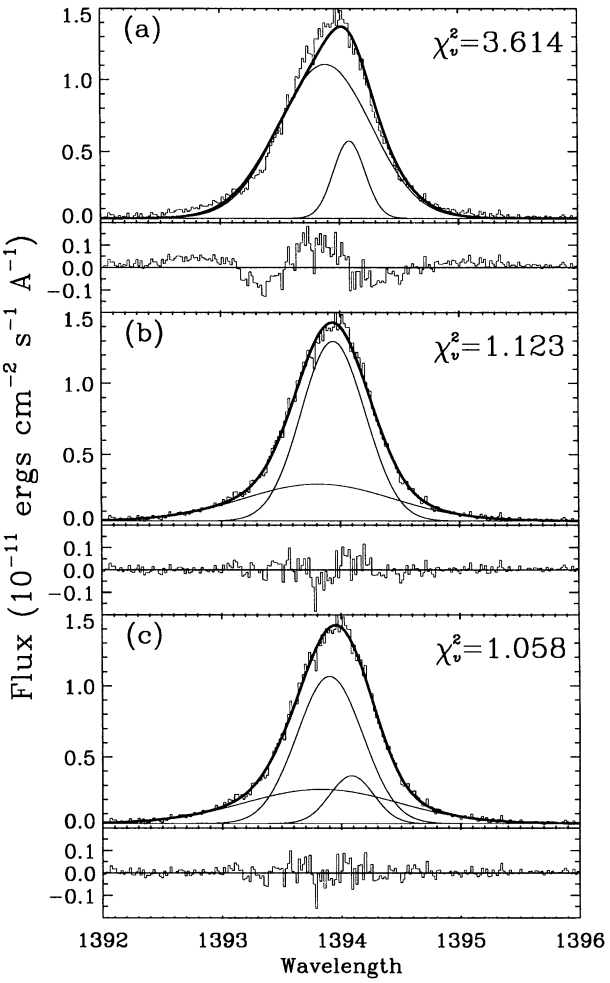

FIG. 7.—Three fits to the Si IV 1393.8 Å line, with the residuals shown below the fits. Panel (*a*) shows a two-Gaussian fit with an H and a C component, where the C component has been required to have a velocity of +15 km s^{-1} with respect to the G8 star. Panel (*b*) shows a two-Gaussian fit with an H and a B component, and panel (*c*) shows the best fit with all three components.

widths of the H, C, and B components of C IV are individually broader than the thermal and instrumental widths. The C IV and Si IV line flux ratios, $f_{1548}/f_{1550} = 1.80$ and $f_{1393}/f_{1402} = 1.75$ as computed from the total line fluxes in Table 3, are smaller than 2.0, which is the observed solar value and the ratio of collision strengths for both the C IV and Si IV lines, assuming LS coupling. This indicates that the lines are moderately optically thick, as are the individual components, since the C IV line flux ratios for the H and B components (Table 4) are 1.71 and 1.86, respectively; while the Si IV line flux ratios for the H and B components are 1.67 and 1.86, respectively. While opacity must have some role in broadening the stronger lines, turbulence likely is the largest contributor to the line width.

The integrated O I line flux for the G1 star is 2.3 times larger than that of the G8 star (flux-weighted average of the three O I lines in Table 4), whereas Ayres (1988) deduced a ratio of 3.6 from much lower quality *IUE* spectra obtained at opposite quadratures. Table 3 shows that the C I and S I lines, which do not have sufficient flux for a multi-Gaussian analysis, have smaller redshifts than the O I lines. This could be explained by either (a) the G8 star does not contribute proportionally as much flux to the C I and S I lines as it does to the O I lines, or (b) the G1 star emission in the C I and S I lines is not as redshifted as it is for O I (+9 km s^{-1} with respect to the G1 star). Based on the work of Wood & Ayres (1994), we believe that case (a) is correct: the G8 star is not as important a flux contributor to the C I and S I lines as it is to the O I lines. Even though the S I lines are pumped by the O I lines, the precise wavelengths and widths of these O I lines are critical to the pumping efficiency.

The ratios of the G1 star flux to the G8 star flux for the C IV 1548.2 Å, Si IV 1393.8 Å, Si III 1206.5 Å, and N V 1238.8 Å lines are 11.8, 7.2, 5.8, and 2.7, respectively. For comparison, Ayres (1988) found values of 10.0, 6.7, 7.7, and ≥ 5 for these ratios. The agreement is good for C IV, Si IV, and Si III, but discrepant for N V. Although Ayres (1988) had observations at both quadratures, the quality of the *IUE* data hindered this work. In particular, the GHRS spectra demonstrate that the G1 star profiles are not Gaussian in shape, especially for the Si III line which has a central reversal. This likely accounts for the difference between our result for N V and that of Ayres (1988), where both the B/H and C/H component ratios are largest.

The large contribution of the G8 star to the N V 1238.8 Å line flux is unexpected given its small contribution to C IV 1548.2 Å. A likely explanation is that the nitrogen abundance is elevated in the G8 star compared with the G1 star owing to the former's more advanced evolutionary state. Nitrogen enrichment can accompany first dredge up at the base of the red giant branch (e.g., Lambert & Ries 1981). Further evidence is the significantly higher redshift of the N I 1411.9 Å line (see Table 3) than for the C I and S I lines, indicating that the G8 star may also be a strong contributor to the N I line. Our emission measure analysis (§ 7) also supports the conclusion. The use of the N V and C IV lines as abundance indicators has been proposed by Böhm-Vitense & Mena-Werth (1992). Additional examples of nitrogen abundance anmalies in the postflash "Clump" giants can be found in Ayres et al. (1995).

4.2. *Line Shifts as a Function of Excitation Temperature*

One of the important and unanticipated results from *IUE* was the discovery of redshifted transition region lines from active single and binary stars (e.g., Ayres et al. 1988). While an accelerating outflow can create the appearance of line redshifts for optically thick lines, the optically thin Si III] 1892.0 Å and C III] 1908.7 Å intersystem lines of most stars studied to date also are strongly redshifted, which strengthens the hypothesis that the redshifts for both optically thin and thick lines are produced by downflowing plasma. Hansteen (1993), among others, has discussed the origins of the redshifts seen on the Sun.

The flux-weighted mean velocity of the intersystem lines in Table 3 is 22 $\pm$ 1 km s^{-1}, or 20 $\pm$ 1 km s^{-1} relative to the G1 star. By comparison, the flux-weighted mean velocity of the H component of the permitted transition region lines is 16 $\pm$ 3 km s^{-1} relative to the G1 star (see Table 4). This velocity increases to 19 $\pm$ 3 km s^{-1} if one excludes the very thick Si III 1206.5 Å line. The close agreement of the mean velocities of the optically thin intersystem lines and the H components of the optically thick permitted lines argues in favor of downflows in the bulk of the plasma where the transition region lines form. The comparison is only valid, however, if the intersystem lines

do not have significant B or C components. Ayres (1988) and Wood & Ayres (1995) have shown that the G1 star accounts for at least 90% of the flux in the Si III] 1892.0 Å, C III] 1908.7 Å, and O III] 1666.2 Å lines, indicating that the C component is negligible, and we see no evidence for very broad wings in the intersystem lines due to a B component. However, all of the strong intersystem lines we have observed either lie on uneven continua or are blended with other lines, rendering broad components hard to detect. The widths of the intersystem lines are similar to those of the H components of the permitted lines, suggesting that the intersystem lines probably lack prominent B components.

Ayres et al. (1988) reported that Capella's density sensitive C III] 1908.7 Å line is less redshifted than the Si III] 1892.0 Å line by about 6 km s^{-1}, which they suggested could imply that the downflows occur in regions of enhanced density. When we initially fit these lines using our GHRS data, we found a similar difference between the two redshifts, but we found no difference between the velocities of the two lines (see Table 3) after we subtracted the simulated photospheric spectrum. The reason is that the photospheric spectrum is brighter on one side of the line that the other (see Fig. 3). While there may be inaccuracies in our synthetic photospheric spectrum, we conclude that the velocity difference reported by Ayres, Jensen, & Engvold (1988) probably is not intrinsic to the Si III] and C III] emission lines.

We find in general that the transition region lines are more highly redshifted than the low-excitation lines (see Tables 3 and 4), as did Ayres (1988). However, our division of the G1 star's transition region line emission into two components (H and B) with different wavelengths makes it difficult to establish a single velocity for the G1 star's lines. Furthermore, the transition region lines analyzed in this paper have surprisingly different properties.

Not only does the behavior of the C IV 1548.2 Å line differ from that of the N V 1238.8 Å line, for example, but it also differs from C IV 1550.8 Å, the other member of the multiplet. In particular, the C IV 1548.2 Å H component has a much smaller redshift than the C IV 1550.8 Å H component. Similar phenomena have been noted in *IUE* data for Capella (Ayres 1988) and for other stars (Ayres et al. 1988). One possible way to explain the difference between these two very similar lines is to appeal to an opacity effect. A decelerating downflow in the portion of the transition region producing the C IV emission could produce a C IV 1550.8 Å line that is redshifted relative to the more optically thick C IV 1548.2 Å line, as suggested by Ayres (1988).

How then can one explain why the Si IV 1402.8 Å H component is *blueshifted* relative to the more optically thick Si IV 1393.8 Å H component? The difference between the velocities of the two Si IV lines is seen in *IUE* data as well (Ayres 1988). Perhaps such velocity differences are produced by blends which subtly alter the C IV and Si IV line profiles. Possible culprits are lines of Fe II and CO. Johansson (1983) found evidence that the C IV 1548.2 Å line is fluorescing Fe II lines in the *IUE* spectra of RR Tel and V1016 Cyg, and Jordan et al. (1979) found evidence that the CO lines in sunspots are fluoresced by all four of the C IV and Si IV lines.

4.3. *The Very Broad Components of the Transition Region Resonance Lines*

One of the significant new discoveries obtained from GHRS spectra is that the transition region lines of active late-type stars have very broad wings that can be fitted with very broad Gaussian components. Linsky & Wood (1994) first discovered very broad wings in the C IV and Si IV lines of the very active dM0e star AU Mic. After fitting each of these lines with a very broad and a narrow component, they hypothesized the two components are produced on different regions of AU Mic's surface. The present paper provides evidence that Capella's transition region lines also have very broad wings. We have modeled these wings with Gaussians, and believe that the G1 star is responsible for these components, as it also is responsible for most of the flux in Capella's transition region lines.

Linsky & Wood (1994) proposed that the very broad components are stellar analogs for solar "transition region explosive events (TREEs)" (see Dere, Bartoe, & Bruckner 1989) for which the very broad profiles are due to the acceleration of plasma away from the heating site. Solar explosive events can be thought of as "microflares," since like flares they are short-lived phenomena thought to be caused by magnetic reconnection. While Capella's G1 star and AU Mic differ in many respects, they have nearly identical C IV and Si IV surface fluxes, implying similar surface-averaged transition region heating rates. However, AU Mic shows rotational modulation (Pettersen 1983) but Capella's G1 star does not (Ayres 1988). This suggests that there are only a few large active regions on AU Mic, while Capella's G1 star probably has numerous small active regions randomly distributed over its surface.

There seems to be a correlation between the temperature of line formation and the strength of the G1 star's B component. The two lines formed at the highest temperatures in the transition region, N V 1238.8 Å and C IV 1548.2 Å (the more optically thick of the two C IV lines), have B components with the largest fraction of the total line flux, while the B component of the lowest excitation transition region line, Si III 1206.5 Å, contains the smallest fraction of the total line flux. The low excitation O I lines and He II 1640.4 Å show no obvious B component at all. We believe that the correlation of line temperature and B component strength is consistent with a vigorous "microflating" heating of the transition region plasma, producing an emission measure distribution skewed to higher temperatures (see § 7).

There also may be a correlation between the optical depth of the lines and the Doppler shift of the B components relative to the H components, although the reality of the correlation is tempered by our lack of a reliable assessment of the errors in the line component velocities. Most of the transition region lines have B components that are slightly blueshifted with respect to the H components. (The flux-weighted average velocity for the B component is 10 ± 4 km s^{-1} compared with 16 ± 3 km s^{-1} for the H component, where again we give the standard error of the mean.) However, the two lines with the largest optical depths, Si III 1206.5 Å and C IV 1548.2 Å, show almost no shift between the H and B components. The Si IV 1402.8 Å and N V 1238.8 Å lines, which have the lowest optical depths of the transition region lines, have B components that are blueshifted by about 17 and 33 km s^{-1} relative to the H components. We have no convincing explanations for this behavior.

4.4. *Profile of the* He II 1640.4 Å *Line*

Figure 4*f* shows the region of the He II 1640.4 Å multiplet observed with the G160M grating. The line appears as a very broad feature with a narrow emission component located about +0.20 Å from the main feature. Three known lines

potentially could be blended with the He II line—Fe II 1640.15 Å seen in solar spectra (e.g., Feldman et al. 1975); O I 1641.305 Å prominent in the spectrum of Arcturus (Ayres, Simon, & Linsky 1982), an inactive K giant; and S I 1641.085 Å. We see no evidence for the Fe II line. Some excess emission appears in the far red wing of the He II line which conceivably could be due to the O I and/or the S I line. However, neither can account for the narrow emission component since both fall well to the red. We therefore adopt the working hypothesis that the narrow component is emission from He II produced by the G1 and/or the G8 star.

The seven components of the He II multiplet, with laboratory wavelengths between 1640.332 and 1640.533 Å, are the Hα lines of hydrogen-like helium produced by permitted transitions between the 2*s* or 2*p* and the 3*s*, 3*p*, and 3*d* states. Considerable effort has gone into explaining the origin of the He II Hα feature in the spectra of the Sun and late-type stars (e.g., Athay 1988; Wahlstrøm 1992). Two alternative models have been developed. The collisional excitation scenario discussed by Jordan (1975) explains the Hα line by electron collisional excitation from the ground state at temperatures of roughly 80,000–125,000 K in the transition region. The radiative recombination model, discussed by Zirin (1975), explains the line as a result of photoionization of He^+ by coronal radiation below 228 Å followed by recombination and cascade at low temperatures near 10,000 K. The collisional excitation model produces a broad Gaussian-shaped profile centered on the laboratory wavelength of 1640.438 Å (Feldman et al. 1975), whereas the recombination model produces two narrow emission features, the strongest being the $2p\,^2P_{3/2}$–$3d\,^2D_{5/2}$ transition at 1640.474 Å. The relative strength of the individual recombination lines depends on the importance of resonance trapping of the He II Lβ line at 256 Å, which can selectively overpopulate certain of the upper states of the Hα line. These and subsequent analyses indicate that a broad emission component can be explained most easily by a collisional excitation model, whereas narrow emission features can only be explained by a radiative recombination model. Wahlstrøm & Carlsson (1994) conclude that for the Sun coronal radiation photoionization followed by cascade recombination is the dominate contributor to the 1640 Å line, but collisional excitation at a temperature of 70,000 K also contributes.

We now propose an explanation for the observed 1640.4 Å feature within this conceptual framework. The observed feature can be well fitted by two Gaussians. The fluxes and FWHM of these are listed in Table 4, together with the radial velocities relative to the mean laboratory wavelengths for the collisional excitation picture and the dominant line in the recombination picture. We assign the narrow line to the G8 star because the observed velocity of 62 km s^{-1} is close to the photospheric radial velocity of the G8 star (55.6 km s^{-1}). At the temperature where He II is formed in the recombination scenario ($T \sim 10{,}000$ K), the expected thermal width is 10.7 km s^{-1}, which is only slightly lower than the measured width of 11.2 km s^{-1} for the narrow component. However, the measured width is uncertain since it is smaller than the instrumental resolution. The broad line likely is formed predominantly on the G1 star, because the radial velocity of 34 km s^{-1} is close to the velocity of the Si IV and C IV lines which form at temperatures similar to that of He II in the collisional excitation picture. Some of the flux in this component may be from the G8 star, however, since Ayres (1988) has estimated from *IUE* opposite quadrature data that the G8 star produces about 20% of the He II emission and the very narrow component contains only about 10% of the He II flux (see also Wood & Ayres 1995).

Our interpretation that the recombination picture is appropriate for the G8 star but not the G1 star is sensible only if the transition region densities in the G1 star are significantly larger than for the G8 star and the EUV illumination is proportionately less, so that collisional excitation dominates in the G1 star but not the G8 star. As we will see in § 7, this is reasonable on both counts. Dupree et al. (1993) estimated that the recombination component of the He II 1640.4 Å line should have a flux of 1.6×10^{-12} ergs cm^{-2} s^{-1} on the basis of the observed extreme ultraviolet flux observed by *EUVE*. Their estimate may be compared with the observed flux of 7×10^{-13} ergs cm^{-2} s^{-1} in the narrow component formed on the G8 star.

4.5. *The* O I *Resonance Lines*

In addition to H and C components, the fit to the I I 1302.2 Å line required a third Gaussian to account for the interstellar absorption present in this line, and a fourth Gaussian to represent the S I line in its red wing. The heliocentric radial velocity of the interstellar feature is 24.5 ± 1.9 km s^{-1}, where the 1 σ error has been estimated using a series of simulations. It is comparable to the interstellar flow velocity of 22.2 ± 1.5 km s^{-1} derived by Linsky et al. (1993a) from GHRS echelle spectra of the Capella Mg II and Fe II lines, the value of 20.0 km s^{-1} for the Capella line of sight predicted using Crutcher's (1982) mean local interstellar medium flow vector, and the 20 ± 1 km s^{-1} derived by Ayres (1988) from *IUE* spectra calibrated using the known γ-velocity of the Capella system (Batten, Hill, & Lu 1991).

The width of the fitted interstellar O I absorption feature at 1302.2 Å is FWHM = 0.050 Å. When the feature is fitted without correcting for the instrumental profile, we find FWHM = 0.098 Å. The difference between these FWHM values implies an effective instrumental width of 0.084 Å and a resolving power of 15,000, compared to the value of 20,000 measured for the SSA (GHRS Instrumental Handbook V4.0). The reduction in effective resolution is due to the non-Gaussian nature of the aberrated instrumental profile, but the complex core/halo shape of the aberrated beam produces a blurred profile that cannot be accurately described by one number. The analysis of the interstellar feature will be published elesewhere.

The line flux ratios for the O I 1302:1305:1306 multiplet should lie between the optically thin limit of 5:3:1 and the optically thick limit of 1:1:1, in the absence of transfer effects other than in the lines themselves. In fact, the line ratios are close to 1:1:1, as expected for resonance lines of an abundant species, but the O I 1306.0 Å line is slightly stronger than the O I 1304.9 Å line in both the G1 and G8 stars, contrary to the prediction for optically thick lines. That behavior also is seen in a more exaggerated way in the spectra of α Boo (K2 III; Ayres et al. 1982), β Dra (G2 II–Ib; Brown et al. 1984), and other late-type giants and supergiants. The anomalous behavior probably is due to the effects of an overlapping continuum (Si I is probably the strongest continuum source), and blends with the S I UV 9 multiplet and to a lesser extent Fe II and other lines. We already have called attention to the S I 1302.9 Å line (probably blended with the 1303.111 Å line of the same multiplet) which is well separated from O I 1302.2 Å with 11% of the latter's flux. Another member of the same S I multiplet with similar line strength lies at 1305.883 Å, which is nearly

coincident with the O I 1306.0 Å line (see Brown & Jordan 1980). Since the S I and O I lines cannot be separated, the cited fluxes for the O I 1306.0 Å line must be decreased by roughly 10%, which brings the O I 1305:1306 line ratio down to the expected optically thick value. Also, the O I 1304.9 Å line may be blended with the Si II 1304.37 Å line (see Jordan & Judge 1984).

5. ANALYSIS OF THE HIGH DISPERSION PROFILES OF THE Mg II *h* AND *k* LINES

Our SSA echelle observations include spectra of the Mg II resonance lines with the unprecedented resolving power of $\lambda/\Delta\lambda = 85{,}000$ (see Linsky et al. 1993a). These are the only lines that we were able to observe at both orbital phases ($\phi = 0.26$ and $\phi = 0.80$), with the exception of the Lyman-α line which is not discussed in this paper. The spectra of the *k* line (rest wavelength of 2795.528 Å in air) and the *h* line (rest wavelength of 2802.705 Å) are shown at both orbital phases in Figure 8. The high spectral resolution and signal-to-noise of these data allow us for the first time to resolve the central reversals of the chromospheric emission lines from both stars and to separate them from the very deep and narrow interstellar absorption lines. Previous studies of the Mg II lines at many orbit phases (Ayres 1984, 1988) were able to separate only partially the chromospheric self-reversals from the interstellar absorption components.

When comparing the two Mg II spectra obtained at different orbital phases, we found a major discrepancy in the Mg II fluxes and a minor discrepancy in the wavelengths of the narrow interstellar medium (ISM) absorption lines in both Mg II lines. Since the Mg II flux from Capella and the ISM velocity along its line of sight should not vary on timescales of decades, we believe these discrepancies indicate calibration problems. The Mg II fluxes in our $\phi = 0.26$ observation are almost a factor of 2 smaller than in the $\phi = 0.80$ observation. Comparison with *IUE* data allows us to conclude with confidence that the $\phi = 0.26$ observation is anomalous. It is possible that the star was partially outside the SSA at the time of that observation, but we cannot be certain because the Lyman-α spectrum also taken through the SSA does not show a similar problem. Before analyzing the Mg II spectra, we forced the $\phi = 0.26$ observation's fluxes to agree with those at $\phi = 0.80$ by multiplying the $\phi = 0.26$ fluxes by a factor of 1.9.

The ISM absorption lines in the $\phi = 0.80$ spectrum are blue-shifted by about 1.8 km s^{-1} with respect to the ISM lines in the $\phi = 0.26$ spectrum. Because there was insufficient time to do a

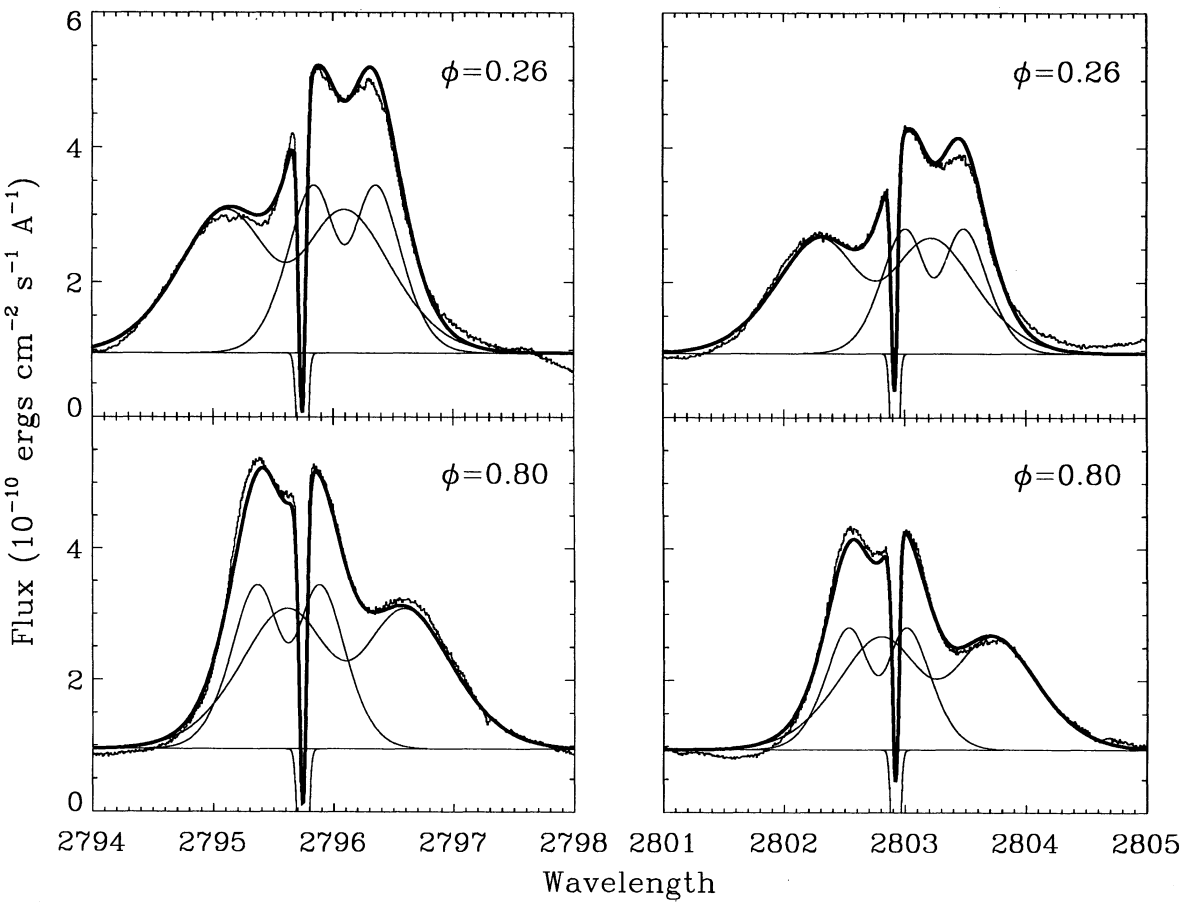

FIG. 8.—Observed profiles of the Mg II *k* line at 2795.5 Å and the Mg II *h* line at 2802.7 Å, which were observed at orbital phases 0.26 and 0.80. The Mg II lines were each fit with five Gaussians—two emission Gaussians representing emission from the two Capella stars, two absorption Gaussians to represent the central absorption at the center of both emission components, and one absorption Gaussian for the narrow ISM absorption feature seen in each Mg II line. Since we know the shift of each component between $\phi = 0.26$ and $\phi = 0.80$, we modeled the $\phi = 0.26$ and $\phi = 0.80$ spectra simultaneously. The thin solid lines represent the individual components (the central reversal Gaussians have been added to their corresponding emission Gaussians), and the thick solid lines are the sum of the components.

wavelength calibration image before the $\phi = 0.80$ observation, unlike the $\phi = 0.26$ observation, we assumed that the calibration of the $\phi = 0.26$ spectrum was the more accurate, and we shifted the $\phi = 0.80$ spectrum by 1.8 km s^{-1} to obtain agreement. Thus the $\phi = 0.26$ spectrum was used to calibrate the wavelengths of the $\phi = 0.80$ spectrum, and the $\phi = 0.80$ spectrum was used to calibrate the fluxes of the $\phi = 0.26$ spectrum.

To estimate the relative contribution of each star to the composite line profiles we fitted the *h* or *k* line profiles with five Gaussians. In each fit, two emission Gaussians represent the emission from each star, two absorption Gaussians represent the central reversals in those emissions, and one narrow absorption Gaussian represents the ISM absorption. The Gaussians simulating the central reversals were forced to have the same central wavelength as the emission Gaussians, but all other parameters were allowed to vary. Again, the most compelling reason for choosing Gaussian shapes for the emission and absorption portions of the line profiles was expedience. We fitted the $\phi = 0.26$ and $\phi = 0.80$ spectra simultaneously, using the known wavelength shifts for the G1 and G8 star components between the $\phi = 0.26$ and $\phi = 0.80$ spectra. Figure 8 depicts the resulting fits. The Gaussian parameters of the fits are given in Table 4 (except for the Gaussians representing the ISM absorption, which we will present elsewhere), where the wavelengths given in the table are for the $\phi = 0.26$ spectrum. We believe we have reliably dissected the Mg II lines into the G1 and G8 star components, but unlike the fits to the moderate resolution lines, these fits are far from 2 σ. In the fits, we have assumed that the continuum is flat and that the very optically thick Mg II emission is Gaussian, but neither of these assumptions is strictly correct.

These data show unambiguously that both stars have central reversals in their Mg II lines. Our model also suggests that Mg II lines both of stars are slightly redshifted by 3–6 km s^{-1}. The G1 star is responsible for about 61% of the emission in the *h* line and 64% of the emission in the *k* line, but these values may be a lower limit since we have excluded any possible contribution of the net flux below the h_1 and k_1 features (see Linsky & Ayres 1978). By comparison, Linsky et al. (1993) determined that the G1 star accounts for about 61% of the observed H I Lyman-α line. Considering all the chromospheric lines together, there seems to be a tendency for the G8 star's contribution to decrease with decreasing line opacity from about 40% for the highly optically thick Lyman-α and Mg II lines to about 30% for the moderately optically thick O I lines, to possibly 25% or less for the much weaker C I and S I lines (see § 4.1).

Finally, it has long been known that there is a strong correlation between stellar luminosity and the width of the Ca II H and K lines, known as the Wilson-Bappu effect (Wilson & Bappu 1957). The Mg II *h* and *k* lines follow a similar correlation (Kondo, Morgan, & Modisette 1976). Because the two Capella stars have nearly identical luminosities, our fits of the Mg II lines are inconsistent with the Wilson-Bappu effect: the G1 star contribution is almost twice as wide as that of the G8 star. Rotational broadening cannot account for this large difference. The width-luminosity correlation of Vladilo et al. (1987) suggests that the G1 star rather than the G8 star is inconsistent with the Wilson-Bappu relation, another example that the G1 star's emission lines are abnormally broad. Other stars inconsistent with the Wilson-Bappu effect are discussed by Ayres (1980).

6. LINE SURFACE FLUXES FOR CAPELLA AND OTHER STARS

The moderate and high dispersion spectra have allowed us to infer the relative contributions to the observed emission line fluxes of each star in the Capella system. We can convert the observed fluxes to surface fluxes given the distance to Capella and the radii of both stars. The ratio of surface flux to observed flux is $F_*/f_* = (d/R_*)^2$, where d is the distance and R_* is the radius of the G1 or G8 star. According to Hummel et al. (1995), the distance to Capella is $d = 13.3 \pm 0.1$ pc, the radius of the G1 star is $R = (6.40 \pm 0.28) \times 10^{11}$ cm, and the radius of the G8 star is $R = (8.49 \pm 0.14) \times 10^{11}$ cm. These parameters lead to $F/f = (4.11 \pm 0.22) \times 10^{15}$ for the G1 star and $F/f = (2.34 \pm 0.08) \times 10^{15}$ for the G8 star. The line surface fluxes listed for the two Capella stars in Table 5 were computed using these ratios. In calculating the surface fluxes for the two Capella stars, we divided the observed C IV, Si IV, O I, and Mg II fluxes between the two stars as indicated in Table 4. For Si III] and C II, we assumed that the G8 star was responsible for only 10% of the emission, consistent with the results of Wood & Ayres (1995). We have in this paper estimated that the G8 star is responsible for only about 25% or less of the observed flux in many C I and S I lines, so we have assumed that the G8 star produces 25% of the observed C I 1657 Å flux in computing the C I 1657 Å surface fluxes listed in Table 5.

We now can compare the line surface fluxes of the two Capella stars to those of other stars as a quantitative measure of the radiative loss rates in the individual lines. For those stars for which we do not have accurate values of the radius and distance, we can determine the surface fluxes by dividing the observed fluxes by the square of the stellar angular radius. The latter may be inferred from the stellar visual magnitude and color (Linsky et al. 1979). The Capella surface fluxes for important lines are given in Table 5, together with corresponding values for the more active RS CVn system, V711 Tau (Byrne et al. 1987), the quiet Sun (Ayres, Marstad, & Linsky 1981), the very inactive K giant Arcturus (α Boo; Ayres et al. 1982, 1995), and the inactive hybrid star γ Dra (Linsky, Wood, & Brown 1993b). Mg II and other chromospheric line fluxes were

TABLE 5

COMPARISON OF EMISSION LINE SURFACE FLUXES (log Units)

Multiplet	log *T*	Saturation Limit	V711 Tau (RS CVn)	Capella (G1 III)	Capella (G8 III)	Sun (G2 V)	γ Dra (K5 III)	α Boo (K2 III)
C IV 1549 Å	5.0	6.2	5.62	5.24	3.89	3.73	2.08	2.02
Si IV 1394 Å.....	4.8	...	5.05	4.66	3.56	3.37	1.60	<1.87
Si III] 1892 Å.....	4.6	...	4.68	4.98	3.79	...	...	1.82
C II 1334 Å.....	4.3	...	5.46	5.00	3.80	3.67	1.93	2.27
O I 1304 Å	3.9	...	5.24	5.01	4.41	3.62	3.70	3.73
C I 1657 Å	3.8	...	5.07	4.56	3.84	...	2.51	2.84
Mg II 2800 Å.....	3.8	7.2	6.82	6.45	5.98	6.07	4.73	5.25

obtained from Ayres et al. (1982) and Simon, Linsky, & Stencel (1982). We also list the maximum observed C IV and Mg II surface fluxes for the youngest and most rapidly rotating stars without circumstellar disks. Vilhu (1987) calls these fluxes "saturated" as they represent the maximum radiative emission from a star completely covered with "active regions."

The data in Table 5 indicate that the surface fluxes of the high-temperature lines for the Capella G1 star lie about a factor of 10 below the saturated limit, if the C IV line is a good guide, and those for the hyperactive V711 Tau system lie even closer to this limit. A natural explanation for this behavior is that a large fraction of the surface area of these active stars is covered by "plages" where the magnetic fields are strong and the heating rate is near its maximum possible value. Indeed, large plages have been identified on the surface of AR Lac by Doppler imaging techniques (Neff et al. 1989), and Linsky (1990) has shown that the surface fluxes in the plages of the RS CVn systems AR Lac, II Peg, and V711 Tau are near the "saturated" limit. Unlike the hyperactive RS CVn binaries, however, the fluxes of Capella's emission lines do not vary with rotational phase, indicating that the G1 star has either a much larger number of active regions or a much higher filling factor, and thus a much lower average heating rate in the active regions than is true on the Sun.

On the other hand, the surface fluxes for the high-temperature lines of γ Dra and α Boo lie a factor of 10,000 below the "saturated" limit. These are the smallest C IV surface fluxes ever measured on a cool star. One could interpret the very small surface fluxes of high-temperature lines on γ Dra and α Boo as indicating that the fraction of the surface of such slowly rotating inactive stars covered by magnetically heated active regions is $\sim 10^{-4}$, much less than the plage and network coverage of the quiet Sun. Alternatively, the heating may be due to acoustic waves generated by convective motions in the photosphere. Cuntz (1987) and Cuntz & Luttermoser (1990) have computed models for α Boo in which a stochastic distribution of acoustic wave periods leads to the occasional coalescence of individual shocks into very strong shocks that produce small amounts of high-temperature plasma.

The cooler star in the Capella system has chromospheric and high-temperature line surface fluxes midway between the two extreme cases of V711 Tau and γ Dra or α Boo, and nearly the same as the Sun. Although only as active as our relatively inactive Sun, the Capella G8 star is among the most active of the single Clump giants (e.g., Ayres 1988).

7. PHYSICAL PROPERTIES OF THE TRANSITION REGIONS DETERMINED FROM THE EMISSION LINE FLUXES

We adopt an "empirical" method for the analysis of emission line surface fluxes in which we make assumptions concerning the processes responsible for spectral line formation and then infer properties of the emitting structures by comparing observed and computed line fluxes. More theoretical approaches (e.g., ab initio methods) are not yet warranted, because overly restrictive assumptions would be required to solve the momentum and energy equations. Techniques for determining physical properties of transition region plasmas using emission line surface fluxes or intensities, including emission measure analysis, have been employed for several decades (e.g., Jordan & Wilson 1971; Jordan & Brown 1981). These methods have the advantage of being simple, but they neglect potentially important physical processes in the calculation of the atomic number densities. Two critical assumptions made almost universally are (i) the neglect of time-dependent terms in the atomic rate equations, and (ii) the adoption of single-temperature Maxwellian distribution functions for all particles. Such effects may be important in the solar transition region (e.g., Hansteen 1993; Shoub 1983), but their importance can only be inferred a posteriori from inconsistencies in the emission measure analysis.

7.1. *Emission Measures*

The frequency integrated flux F_{ji} (units ergs cm^{-2} s^{-1}) of an effectively thin emission line between levels j and i of an atom can be written:

$$F_{ji} = \frac{h\nu_{ji}}{2} \int_{\Delta z} \frac{N_j A_{ji}}{N_e^2} N_e^2 \, dz \, .$$

Here N_j (cm^{-3}) is the number density of the upper level, A_{ji} (s^{-1}) is the Einstein A-coefficient of the line for a transition between levels j and i, and N_e (cm^{-3}) is the electron density. The reason for writing the equation in this form is that the ratio $(N_j A_{ji})/N_e^2$ is, to a high degree of approximation, a function only of temperature T_e and N_e. For resonance lines formed at transition region temperatures, this ratio is a weak function of N_e and a strongly peaked function of T_e, say $f(T_e)$. Recognizing this the above equation can be recast into an integral over the variable t (which can be T_e or, more conveniently, $t = \log_{10} T_e$) using the transformation via dz/dt (see Craig & Brown 1976 for a general definition) to give

$$F_{ji} = \frac{h\nu_{ji}}{2} \int_{\Delta t} f(t)\xi(t) dt \, ,$$

where the "differential emission measure" $\xi(t)$,

$$\xi(t) = N_e^2 \, dz/dt \, ,$$

is the quantity which must be integrated over variable t to determine the total emission measure, E_m, for the emitting plasma. This is the "source function" which can in principle be determined (with constraints concerning its "smoothness") from a set of emission line fluxes, by an inversion of the set of corresponding integral equations (either formally, or by performing a least-squares fit to the "forward" problem). Customarily, authors use temperatures falling between $\pm$ a constant in the logarithm of the electron temperature, e.g., $\xi^{0.1}(t)$ is the differential emission measure for all plasma with $t = \log T_e$ in the range $\log T_e - 0.05$ to $\log T_e + 0.05$. This quantity forms the starting point for further modeling (Jordan & Brown 1981).

Before embarking on attempts to determine $\xi(t)$, we can also define a useful quantity, the "emission measure locus" $E_m^{ji}(t)$ (units cm^{-5}) of each line,

$$E_m^{ji}(t) = \int_{\Delta z} N_e^2 \, dz = F_{ji} \Big/ \left(\frac{h\nu_{ji}}{2} \frac{N_j A_{ji}}{N_e^2} \right) .$$

$E_m^{ji}(t)$ represents the amount of isothermal material needed to produce the observed line flux; its relation to the differential emission measure is clarified below. The ratio $N_j A_{ji}/N_e^2$ is computed from solutions to the atomic rate equations, assuming statistical equilibrium, with an assumed elemental abundance and with $N_H = 0.8 N_e$, where N_H and N_e are the total hydrogen and electron number densities, respectively. For permitted lines, $N_j A_{ji}/N_e^2$ depends strongly on t but only weakly on N_e. For collisionally de-excited spin-forbidden lines (i.e., when $N_e C_j > A_{ji}$ and $C_j = \Sigma_i C_{ji}$ cm^{-3} s^{-1} is the total collisional rate out of level j), $N_j A_{ji}/N_e^2 \propto f(t)/N_e$. In this case,

$E_m^{ji}(t)$ is proportional to N_e for $N_e \gg N_e^{cr} = A_{ji}/C_j$ is the "critical electron density."

For a line formed near the peak of the emissivity function $N_j A_{ji}/N_e^2$, $\xi^{0.1}(t)$ can be estimated from the $E_m(t)$ locus via

$$\xi^{0.1}(t)/0.1 \simeq E_m(t = \log_{10} T_0)/\Delta t ,$$

where Δt is the full width at half maximum of the inverse of the $E_m(t)$ loci. Thus, for a line such as C IV 1550 Å, where $\Delta t \sim 0.25$, $\xi^{0.1}(t) \sim E_m(10^5 \text{ K})/2.5$, and the $E_m(t)$ loci can be used to estimate a starting point for determining $\xi(t)$. For other lines (e.g., C II 1334 Å), $\xi(t)$ it must be obtained by an iterative technique (e.g., Jordan & Brown 1981), since the line is formed away from the peak of the emissivity function where the emission measure may be changing rapidly with temperature.

All of the GHRS lines for which reliable atomic data are avaliable were analyzed, as well as the 220.35 Å line of O V obtained by Dupree et al. (1993) from EUVE spectra, for reasons discussed below. Solutions to the multilevel rate equations were obtained for atomic models of C, N, O, and Si, including ionization stages II through VI, using the best available atomic data. Details are presented by Judge & Brekke (1995). The largest sources of uncertainty in these calculations (in addition to systematic errors due to inaccuracies of our basic assumptions) come from the treatment of the ionization balance, since no density dependence of dielectronic recombination rates was included (e.g., Summers 1974). We used the rate coefficients of Arnaud & Rothenflug (1985).

For the Sun and the Capella G1 star we adopted two sets of solar abundances, a "photospheric" set and a "coronal" set, since there is increasing evidence for element separation in the outer solar atmosphere as a function of the element's first ionization potential (FIP). For the "low-FIP" elements (FIP < 10 eV), the solar abundances are a factor of 3 or so higher in the transition region and corona than in the photosphere. We therefore adopted solar photospheric abundances (Grevesse & Anders 1991) of 8.60, 8.00, 8.93, 7.55 for C, N, O, and Si, respectively, on a logarithmic scale where $H \equiv 12$. For our adopted solar "coronal" abundances we set C, N, O to photospheric values and Si to 3 times the photospheric value (Meyer 1995). For the Capella G8 star we also used typical "evolved" abundances for a star having undergone first dredge up (8.35, 8.40, 8.93, 7.55 for C, N, O, and Si, respectively) from Lambert & Ries (1981).

Plotted in Figure 9 are emission measure loci $E_m(t)$ and differential emission measure $\xi^{0.1}(t)$ values for an active region on the Sun (Judge & Brekke 1994) and for five sets of line surface fluxes and assumed abundances for Capella. The differential emission measures were derived simply by adopting a starting $\xi(t)$ function (a line beneath the $E_m(t)$ loci was chosen and smoothed in t), computing theoretical fluxes for the resonance lines, and then iterating to obtain a smooth function which minimizes the square of the difference between observed and computed fluxes. The different line surface fluxes used in the Capella plots come from the summed line fluxes (Tables 2 and 3), and from the fluxes determined from the multiple Gaussian fits of Table 4. In Figure 9, the asterisks indicate permitted lines that have contributions due to collisions from excited levels. Since the density-sensitive lines yield emission measures that are functions of N_e as well as t, only the permitted lines were used to determine $\xi^{0.1}(t)$. $E_m(t)$ curves are shown for the spin-forbidden lines (labeled with "]"), computed in the "low density limit" where $N_e \ll N_e^{cr}$ for all the lines (a value of $N_e = 10^7$ cm^{-3} was used). Table 6 lists values of N_e^{cr} for the spin-forbidden lines. These sometimes differ substantially from earlier calculations (e.g., Doschek 1987) owing to the more recent atomic data used here. For the spin-forbidden lines, $E_m(t) \propto N_e$ when $N_e > N_e^{cr}$.

7.2. *Electron Densities*

Several independent diagnostics are available for determining electron densities of the UV emitting plasmas in our data set.

1. The most reliable diagnostics are ratios of lines within the same multiplet. In particular, ratios of lines within the O IV] $2s^2 2p\ ^2P^o \rightarrow 2s2p^2\ ^4P$ multiplet are excellent diagnostics of electron density in the range $10^9 < N_e < 10^{12}$ cm^{-3} (Judge & Brekke 1995, and references therein), because there are only small uncertainties due to unknown temperatures, ion fractions or elemental abundances. Earlier criticisms by Feldman & Doshek (1979) and others of using such lines were based on two problems. First, the ratios change by only factors of ~ 3 over the whole range of density sensitivity, hence the larger uncertainties in atomic cross sections and oscillator strengths then available led to large and unknown errors in N_e derived from a given observed line ratio. Their second criticism dealt with the low signal/noise of earlier data sets, especially the many analyses using photographic data. Both of these sources of potentially large uncertainties have now been reduced. The two most reliable of the three measured O IV] line ratios yield $N_e \sim (7 \pm 1) \times 10^9$ cm^{-3} (see Table 6), using the fluxes tabu-

TABLE 6

DERIVED ELECTRON DENSITIES ABD PRESSURES

				Total Flux		H Component	
Diagnostic	Method	log $\langle T_e \rangle$ (K)	log N_e^{cr} (cm^{-3})	log N_e (cm^{-3})	log P_e (cm^{-3} K)	log N_e (cm^{-3})	log P_e (cm^{-3} K)
O IV] 1401.1/1407.4 Å.....	Line ratio	5.2	...	9.5:	14.7:	9.5:	14.7:
O IV] 1401.1/1404.8 Å.....	Line ratio	5.2	...	9.8	15.0	9.8	15.0
O IV] 1399.8/1404.8 Å.....	Line ratio	5.2	...	9.9	15.1	9.9	15.1
Si III] 1892 Å/$E_m^{0.1}$	E_m ratio	4.4	10.7	<11	<15.5	<11	<15.5
C III] 1908 Å/$E_m^{0.1}$	E_m ratio	4.7	9.1	10.3:	15	10.3	15
O III] 1666 Å/$E_m^{0.1}$	E_m ratio	4.9	10.6	10.3:	15.2	<10.3	<15.2
N IV] 1486 Å/$E_m^{0.1}$	E_m ratio	5.1	10.1	11:	16.1:	<11	<16.1
O IV] 1401 Å/$E_m^{0.1}$	E_m ratio	5.2	10.8	11.7:	16.9	<11.3	<16.5
O V] 1218 Å/$E_m^{0.1}$	E_m ratio	5.4	10.8	...	...	...	...

NOTES.—A colon marks an approximate value. Line ratios are probably accurate to 0.1 in the logarithm, ratios of emission measures perhaps 0.3 in the logarithm or worse. The first of the listed O IV] line ratios is unreliable because it lies on a "flat" part of the density vs. line ratio curve, where small changes in the line ratio lead to large changes in the derived electron density.

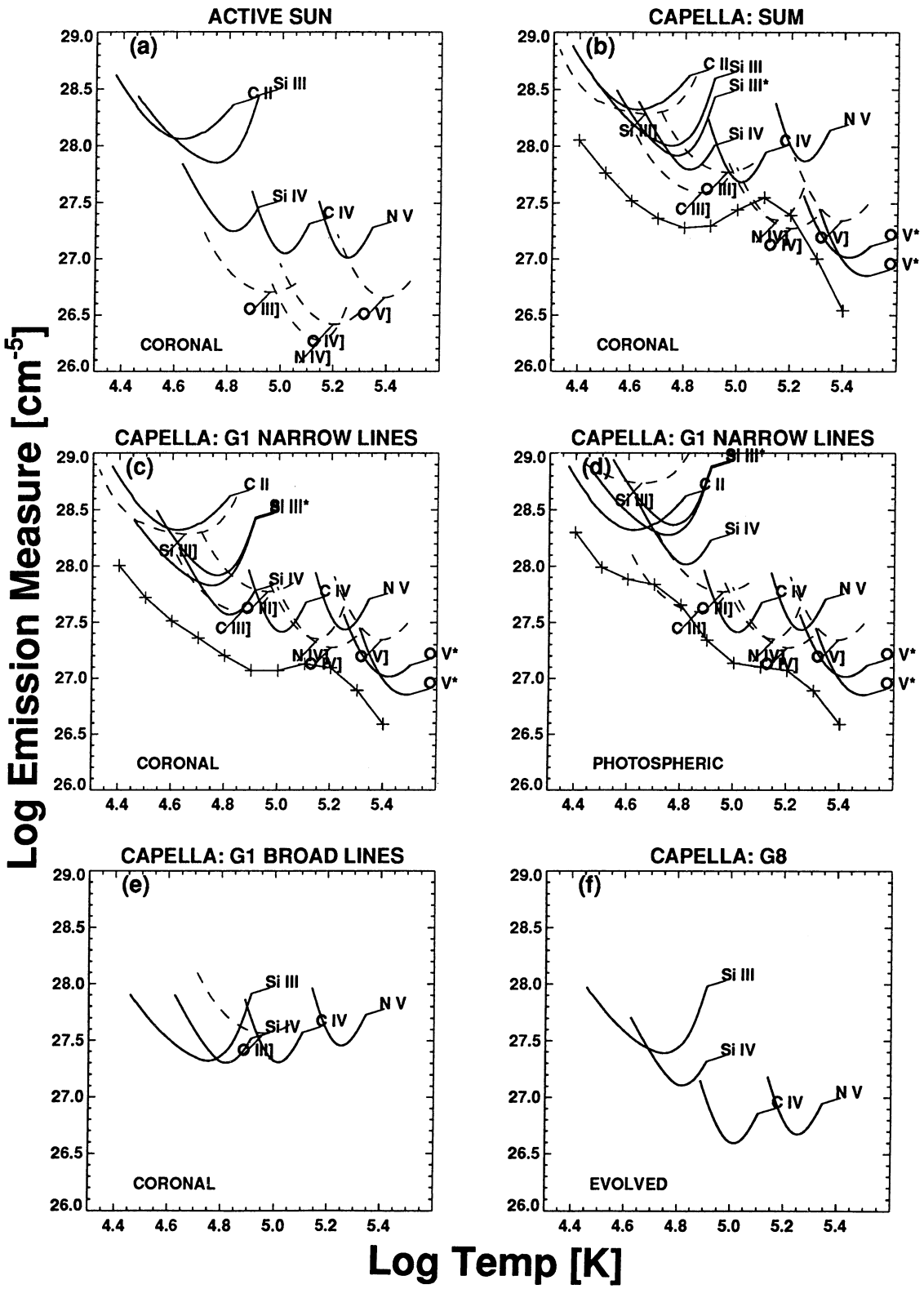

FIG. 9.—Emission measures computed as described in the text. The solid lines show $E_m(T_e)$ loci for permitted lines. These were used to derive the $\xi^{0.1}(t)$ differential emission measures discussed in the text, shown as solid lines with plus symbols. The $\xi^{0.1}(T_e)$ curves lie substantially below the $E_m(T_e)$ loci because the former represent the amount of emitting material in a temperature interval within ± 0.05 in the log of T_e, whereas the latter represent the same thing over roughly the full width at half maximum of the inverse of the $E_m(T_e)$ loci (see text). The dashed lines show emission measure $E_m(T_e)$ loci for the spin-forbidden lines, computed for a "low" value of the electron density (a value of $N_e = 10^7$ cm^{-3} was used). For these lines, the emission measure loci scale linearly with N_e for $N_e > N_e^{cr}$, where the critical electron densities, N_e^{cr}, are listed in Table 6. The set of abundances used are given at the top right-hand corner of each panel.

lated in Table 3. We do not estimate densities using flux ratios of the Al-like S IV] lines because of large uncertainties in the present atomic data (Judge & Brekke 1994). We have argued in § 4.2 that intersystem lines such as O IV] are formed primarily on the G1 star and their widths indicate formation in the H component. One expects the presumably weak C components of O IV] to have some effect on our density determination, though, as the density of the transition region of the G8 star should be lower than for the G1 star. Much deeper spectra are needed to measure possible weak B and C components of these lines.

2. The next most reliable diagnostics are ratios of lines within the same ion but in different multiplets, e.g., Si III] 1892 Å *versus* Si III 1206 Å, and O V] 1218 Å *versus* O V 1371 Å. These diagnostics are less reliable because the line emissivities depend on temperature as well as density, but they can provide independent and accurate electron densities when the differential emission measure distribution is determined accurately.

3. The least reliable diagnostics are ratios of lines with allowed transitions to lines of a different ion stage or element with metastable upper levels. Examples of such line ratios include the fluxes of O III] 1666 Å *versus* Si IV 1402 Å, O IV] 1401 Å *versus* C IV 1550 Å and N V 1240 Å, and O V] 1218 Å *versus* N V 1240 Å. These line ratios are the least accurate density diagnostics because they are susceptible to errors introduced by uncertainties in abundances and ion balance calculations; nevertheless, useful densities can still be obtained when sufficient information on the differential emission measure distribution and abundances is available. A simple interpretation of the data in panels (*a*) and (*b*) of Figure 9 is that the densities in the regions emitting most of the permitted line fluxes (and hence most of the radiative energy from the plasmas) near 10^5 K are in excess of 10^{11} cm^{-3}, because the spin-forbidden transitions would be far stronger if the densities were lower. Note that this density is in stark contrast to the value of 7×10^9 cm^{-3} derived from the O IV] line ratios.

For a homogeneous thermal plasma, these three methods should yield identical electron densities within the uncertainties of the observed data and the atomic excitation calculations. By following a step-by-step approach in which we systematically increase the number of different components assumed to be contributing to the line fluxes, we will demonstrate that the electron densities derived by the various methods are in strongest disagreement when the emission measures are computed from the total line fluxes (Table 3). We can, however, obtain consistent electron densities from the different methods when we consider only the H components of the lines and assume that the spin-forbidden lines do not have B components, which is consistent with the observations reported here. We cannot be certain that the spin-forbidden lines do not indeed have B components, because unfortunately these lines either lie on uneven "background continua" (such as the Si III], C III], O III], and O V] lines) or they are blended with other lines (such as the O IV] lines), which makes it very difficult to identify the wings of these spin-forbidden lines.

7.3. *Analysis of the Total Emission Spectrum of Capella*

Panels (*a*) and (*b*) in Figure 9 provide an interesting comparison between the transition regions of the active Sun and the Capella system, which contains contributions from all three previously identified components: the moderately broad lines from the hotter star (component H), the very broad lines from the hotter star (component B), which we ascribe to microflaring, and the narrow lines for the cooler star (component C). Analysis of the total emission line fluxes will test whether the application of our spectroscopic techniques to the line fluxes from the whole Capella system can yield sensible results when more than one component exists in the emission lines. We will also repeat our analysis considering only the individual component line fluxes to see if this produces more consistent results.

The permitted transitions (*solid lines*) in Figure 9*b* show a very interesting behavior. Below $T_e \sim 1 \times 10^5$ K, the differential emission measure distributions for the active Sun and the Capella system are similar. Above this temperature, the Capella differential emission measures as indicated by the O V* data drop rapidly, consistent with the results of Dupree et al. (1993) based on EUVE and *IUE* data. The solar differential emission measure above $T_e \sim 2 \times 10^5$ K increases according to $E_m(T_e > 2 \times 10^5 \text{ K}) \propto T_e^{3/2}$ up to $T_e \sim 10^6$ K (see the recent review by Mariska 1992). The average energy balance in the upper transition regions of Capella and the Sun are thus very different.

The emission measure loci of the weak O V 1371 Å line and the O V] 1218 Å line show a substantial discrepancy which must be checked using as many independent line ratios as possible, such as the 220.35 Å line of O V, especially since both the 1371 and 1218 Å lines have density-sensitive emissivities. Figure 9*b* shows a potential interesting discrepancy between the permitted lines of N V and O V, and also between N V 1240 Å and O V] 1218 Å. In Figure 9*b* we can see that one cannot construct a reasonable emission measure distribution $\xi^{0.1}(T_e)$ that is consistent with both the O V and N V emission measures when the total line fluxes are used.

On the basis of Figure 9*b*, and without further information on the separate components, one could argue that if all the lines are formed in their low-density limits, then the spin-forbidden lines are too weak relative to the permitted lines. In fact, this analysis requires the existence of multi-density plasmas, since the O IV] density-sensitive ratios yield $N_e \sim 10^{10}$ cm^{-3}, whereas the comparison of the O III], N IV], and O IV] emission measures with those of C IV and N V implies densities in the C IV and N V emitting regions of up to 5×10^{11} cm^{-3}. Densities closer to 10^{10} cm^{-3} are implied by a similar comparison at the lower temperatures of permitted lines of C II, Si III, and Si IV with the C III] and Si III] spin-forbidden lines (see Table 6).

A possible cause of the discrepancy between the intersystem and permitted lines is that the fluxes of the permitted lines contain substantial contributions from the B components, whereas this may not be the case for the spin-forbidden lines. We address this question further in § 7.4. Judge & Brekke (1995) argue that such a discrepancy is not present in the solar data where differences between the solar spin-forbidden and permitted lines (see Fig. 9*a*) probably do indicate multiple-density components in the solar transition region.

7.4. *Analysis of the Spectrum of the G1 Star*

7.4.1. *The Moderately Broad Line Component* H

Panel (*c*) of Figure 9 is the same as panel (*b*) except that we have replaced the total fluxes of the Si III, Si IV, C IV, and N V lines with the H component fluxes of these lines given in Table 4. We do the same in panel (*d*), but we also change the assumed abundances from coronal to photospheric. The most striking features of Figures 9*c* and 8*d* are:

1. A smooth differential emission measure distribution can be constructed from the line fluxes for the permitted transitions (*solid lines*) in panels (*c*) and (*d*). The $\xi^{0.1}(T_e)$ curves are more self-consistent when "coronal" abundances are used (Fig. 9*c*) rather than photospheric abundances (Fig. 9*d*). However, we do not have moderate disperson spectra of the C II 1335 Å multiplet, and thus we cannot determine whether the total line flux we are using for that line in Figures 9*c* and 9*d* is contaminated by a B component. The C II lines are crucial for determining abundance variations between Si (the only "low-FIP" element in our analysis) and the other elements.

2. The discrepancies seen in panel (*b*) between the emission measures of the N V and O IV] lines compared to all of the O V lines are drastically reduced by analyzing line fluxes for the H component only (see Figs. 9*c* and 9*d*).

3. The spin-forbidden line emission measures are consistent with the permitted lines only at low densities: electron densities of about 10^{10} cm^{-3} or less may account for the relative fluxes of all of the spin-forbidden and permitted lines (Table 6). However, if the spin-forbidden lines have strong but undetected very broad components, then the actual H component fluxes and emission measures of the spin-forbidden lines are significantly lower than we have assumed, and higher densities would be implied.

Our data reduction procedure of identifying and separating the three components on the basis of the line profiles and then analyzing the fluxes from each component separately is supported by the unreasonably high densities and inconsistent plasma diagnostics derived from the analysis of the total spectrum and the large contribution to the total N V emission from the C component. These diagnostic results will be the starting point for further modeling of the atmosphere of the G1 star, following the method of Jordan & Brown (1981).

The electron pressures in Table 6 for the H component are consistent with a constant pressure and hydrostatic equilibrium transition region for the G1 star, but this is emphatically not the case in our analysis of the total emission line fluxes. In a later paper, we will consider whether the assumption of hydrostatic equilibrium for the H component is consistent with both coronal emission measures and the transition region pressures derived here.

We call attention to the need for additional data to determine the emission measure distribution above $T_e = 10^5$ K; the N V line appears to be difficult to fit, possibly because of the large contribution of component C in the total Capella emission (Table 4). More data are needed in this temperature region, since it is not now possible to determine whether changes in the emission measure distribution or higher electron pressures are responsible for discrepancies between the $E_m(T_e)$ curves of N V and those of N IV]. O IV] (and to a lesser degree O V] and O V*). For this reason the densities in Table 6 obtained from the emission measures have been flagged as uncertain.

7.4.2. *The Very Broad Line Component* B

Figure 9*e* shows the emission measure loci for the very broad component lines of the G1 star that could be measured. The spin-forbidden line of O III], shown as an upper limit in panel (*e*), is the best candidate for measuring upper limits of fluxes of spin-forbidden lines in the very broad line component because it is not noticeably blended with other lines and it lies on a relatively flat continuum. In the absence of emission measures for low T_e lines like C II, it is not possible to constrain the shape of the differential emission measure distribution beyond the uncertainties of assuming either "coronal" or "photospheric" abundances for the B component. The "coronal" abundance emission measures in Figure 9*e* show a nearly constant distribution, very different from that of the active Sun (Fig. 9*a*), thus requiring relatively little heating near log $T_e \sim$ 4.7 relative to that at log $T_e \sim 5.0$ where C IV is formed. This is reminiscent of the differential emission measure distribution derived from HRTS data of a sunspot by Judge & Brekke (1995). The O III] density-sensitive line, whose locus is an upper limit, produces no constraints on the density of component B. Deeper GHRS exposures are needed to determine whether this line has a B component.

7.5. *Analysis of the Spectrum of the G8 Star (Component* C)

Relatively little can be said concerning the transition region of the G8 star (component C), since no density diagnostics are available and the only measured lines are from both the "low-FIP" ions of Si III and Si IV and the "high-FIP" ions of C IV and N V. It is impossible, therefore, to separate changes in the differential emission measure distribution with temperature from changes in abundances that may result either from the presence of electrodynamical separation processes in the stellar outer atmosphere or from effects of the first dredge up of nuclear processed material. The adoption of "evolved" abundances provides a much better fit to the fluxes derived from the line profile analysis than does the use of solar abundances (not shown). The solar abundances yield emission measures of C IV and N V that are 0.25 dex lower and 0.4 dex higher, respectively, than those shown in Figure 9*f*. The line fluxes would be almost impossible to reproduce using such abundances from any reasonable differential emission measure distribution. The existence of "evolved" abundances on the G8 star is also supported by our result that the data for component H become much more self-consistent when the flux of the N V lines in the C component is enhanced relative to the other lines.

Finally, the lower gravity and lower emission measures in the transition region of the G8 star suggest lower transition region pressures in this star than in the G1 star. Hertzsprung gap giants like the Capella G1 star, however, tend to show coronal X-ray luminosities that are deficient by an order of magnitude or more compared with what would be expected for a Clump giant (like the Capella G8 star) at the same level of C IV emission (e.g., Ayres et al. 1995). Thus the He II recombination mechanism should be relatively enhanced in the G8 star, and suppressed in the G1 star (where collisional excitation would dominate).

8. CONCLUSIONS

Our GHRS study of the Capella system has provided some important insights into the structure of the Capella transition regions which may be representative of active stars in general:

1. Our high-resolution spectra allow us to dissect the composite spectra into the contributions of each individual star. We find that the percent contribution of the hotter star (G1 III) increases from (62 ± 2)% for the Mg II resonance lines and (69 ± 1)% for the O I resonance lines, all formed in the chromosphere, to (88 ± 4)% for the Si III, Si IV, and C IV lines formed in the transition region at temperatures near 10^5 K. The redshifts of the lines formed in the G1 star increase with temperature of formation).

2. The permitted transition region lines assigned to the hotter star on the basis of their Doppler shifts each consist of a

moderately broad and a very broad component. The very broad lines previously seen on the Sun as "transition region explosive events" and in spectra of the dM0e star AU Microscopii are likely due to magnetic field reconnection or microflaring events. The relative importance of the very broad components to the total line flux from the G1 star increases with the temperature of formation.

3. The He II 1640.4 Å multiplet consists of a broad profile and a narrow component. We explain the broad profile as due to collisional excitation in the transition region of the G1 star, and the narrow component as due to radiative recombination in the G8 star's atmosphere.

4. The Mg II resonance lines observed with the echelle grating clearly show self reversals in the profiles of both stars.

5. Emission line surface fluxes for the G1 star are an order of magnitude below the saturation limit, but the emission line fluxes show no evidence for rotational modulation. This suggests that the G1 star is uniformly covered by a large number of active regions. Surface fluxes for the G8 star are more than an order of magnitude smaller than for the G1 star and similar to those of the Sun.

6. We observed spin-forbidden emission lines of C III], O III], Si III], O IV], O V], and S IV] that are sensitive to electron density. These are the highest quality data of this available for any except the Sun. The O IV] line ratios indicate an electron density $N_e \sim (7 \pm 1) \times 10^9$ cm^{-3} for the G1 star's moderately broad component.

7. An emission measure analysis of the total (composite) spectrum does not lead to a self-consistent emission measure distribution, probably because of abundance differences between the G1 and G8 stars and the existence of very broad components in at least some of the lines.

8. An emission measure analysis of the G1 star's moderately broad permitted transition region lines (the H component) leads to a self-consistent model with an electron pressure of $P_e = 10^{15 \pm 0.1}$ cm^{-3} K assuming "coronal" abundances. The H component appears to be close to hydrostatic equilibrium with a constant pressure.

9. The emission measure distribution for the G1 star's very broad component is similar in shape to that of a sunspot, but is very different from that of the G1 star's H component. We conclude that there is relatively little heating near log $T_e \sim 4.7$ relative to that at log $T_e \sim 5.0$ in the B component.

Deeper exposures with the GHRS are needed to provide more information on the three transition-region components in Capella; in particular, one should search for the very broad components of the spin-forbidden lines in the G1 star.

This work is supported by NASA grant S-56500-D to the National Institute of Standards and Technology. We thank Ken Carpenter and Rich Robinson for their advice in the reduction and analysis of these data, and we thank Gary Rottman for his detailed comments on the manuscript. We also thank Glenn Wahlgren for providing us with the model continuum for the 1880–1920 Å spectral region, and an anonymous referee for many useful comments.

REFERENCES

Arnaud, M., & Rothenflug, R. 1985, A&AS, 60, 425
Athay, R. G. 1988, ApJ, 329, 482
Ayres, T. R. 1980, in The Universe at Ultraviolet Wavelengths: The first Two Years of *International Ultraviolet Explorer*, ed. R. D. Chapman (NASA CP 2171), 237
———. 1984, ApJ, 284, 784
———. 1988, ApJ, 331, 467
———. 1991, ApJ, 375, 704
Ayres, T. R., et al. 1995, ApJS, 96, 223
Ayres, T. R., Jansen, E., & Engvold, O. 1988, ApJS, 66, 51
Ayres, T. R., & Linsky, J. L. 1980, ApJ, 241, 279
Ayres, T. R., Marstad, N. C., & Linsky, J. L. 1981, ApJ, 247, 545
Ayres, T. R., Simon, T., & Linsky, J. L. 1982, ApJ, 263, 791
Ayres, T. R., Stencel, R. E., Linsky, J. L., Simon, T., Jordan, C., Brown, A., & Engvold, O. 1983, ApJ, 274, 801
Batten, A. H., Fletcher, J. M., & Mann, P. J. 1978, Pub. Dom. Astrophys. Obs. Victoria, 15, 121
Batten, A. H., Hill, G., & Lu, W. 1991, PASP, 103, 623
Bevington, P. R., & Robinson, D. K. 1992, Data Reduction and Error Analysis for the Physical Sciences (New York: McGraw-Hill)
Böhm-Vitense, E., & Mena-Werth, J. 1992, ApJ, 390, 253
Brandt, J. C., et al. 1982, in The Space Telescope Observatory, ed. D. N. B. Hall (NASA CP 2244), 76
Brown, A., & Jordan, C. 1980, MNRAS, 191, 37P
Brown, A., Jordan, C., Stencel, R. E., Linsky, J. L., & Ayres, T. R. 1984, ApJ, 283, 731
Byrne, P. B., Doyle, J. G., Brown, A., Linsky, J. L., & Rodonò, M. 1987, A&A, 180, 172
Craig, I. J. D., & Brown, J. C. 1976, A&A, 49, 239
Crutcher, R. M. 1982, ApJ, 254, 82
Cuntz, M. 1987, A&A, 188, L5
Cuntz, M., & Luttermoser, D. G. 1990, ApJ, 353, L39
Dere, K. P., Bartoe, J.-D. F., & Brueckner, G. E. 1989, SP, 123, 41
Doschek, G. A. 1987, in Theoretical Problems in High Resolution Solar Physics II, ed. R. G. Athay & D. S. Spicer (NASA CP 2483), 37
Drake, S. A., & Linsky, J. L. 1986, AJ, 91, 602
Duncan, D. K. 1992, Goddard High-Resolution Spectrograph Instrument Handbook, Version 3.0 (Baltimore: STScI)
Dupree, A. K., Brickhouse, N. S., Dosheck, G. A., Green, J. C., & Raymond, J. C. 1993, ApJ, 418, L41
Ebbets, D. 1992, Final Report of the Science Verification Program for the Goddard High-Resolution Spectrograph for the *HST* (Boulder, CO: Ball Corp.)
Feldman, U., & Doschek, G. A. 1979, A&A, 79, 359
Feldman, U., Doschek, G. A., VanHooser, M. E., & Tousey, R. 1975, ApJ, 199, L67
Grevesse, N., & Anders, E. 1991, in Solar Interior and Atmosphere, ed. A. N. Cox, W. C. Livingstone, & M. S. Matthews (Tucson: Univ. Arizona Press), 1222
Hansteen, V. 1993, ApJ, 402, 741
Hassler, D. M., Rottman, G. J., &Orrall, F. Q. 1991, ApJ, 372, 710
Heap, S. R., et al. 1995, PASP, submitted
Hummel, C. A., Armstrong, J. T., Quirrenbach, A., Buscher, D. F., Mozurkewich, D., Elias, N. M., II, & Wilson, R. E. 1995, AJ, in press
Jenkins, E. B. 1987, in Interstellar Processes, ed. D. H. Hollenbach & H. A. Thronson, Jr. (Drodrecht: Reidel), 533
Johansson, S. 1983, MNRAS, 205, 71P
Jordan, C. 1975, MNRAS, 170, 429
Jordan, C., Bartoe, J.-D. F., Brueckner, G. E., Nicolas, K. R., Sandlin, G. D., & VanHooiser, M. E. 1979, MNRAS, 187, 473
Jordan, C., & Brown, A. 1981, in Solar Phenomena in Stars and Stellar Systems, ed. R. M. Bonnet & A. K. Dupree (Dordrecht: Reidel), 199
Jordan, C., & Judge, P. 1984, Phys. Scripta, T8, 43
Jordan, C., & Wilson, R. W. 1971, in The Physics of the Solar Corona, ed. C. J. Macris (Dordrecht: Reidel), 219
Judge, P., & Brekke, P. 1995, in preparation
Kelly, R. L. 1987, J. Phys. Chem. Ref. Data, 16, Suppl. No. 1
Kondo, Y., Morgan, T. H., & Modisette, J. L. 1976, ApJ, 207, 167
Lambert, D. L., & Ries, L. M. 1981, ApJ, 248, 228
Lenz, D. D., & Ayres, T. R. 1992, PASP, 104, 1104
Linsky, J. L. 1990, in Active Close Binaries, ed. C. Ibanoglu (Dordrecht: Kluwer Academic), 747
Lynsky, J. L., & Ayres, T. R. 1978, ApJ, 220, 619
Linsky, J. L., et al. 1993a, ApJ, 402, 694
Linsky, J. L., & Wood, B. E. 1994, ApJ, 430, 342
Linsky, J. L., Wood, B. E., & Brown, A. 1993b, in Science with the *Hubble Space Telescope*, ed. P. Benvenuti & E. Schreier (Garching: ESO), 287
Linsky, J. L., Worden, S. P., McClintock, W., & Robertson, R. M. 1979, ApJS, 41, 47
Maran, S. P., et al. 1994, ApJ, 421, 800
Mariska, J. T. 1992, The Solar Transition Region (Cambridge: Cambridge Univ. Press)
Meyer, J.-P. 1995, in Origin and Evolution of the Elements, ed. N. Prantzos, E. Vangioni-Flam, & M. Cassé (Cambridge: Cambridge Univ. Press), in press
Morton, D. C. 1991, ApJS, 77, 119

Neff, J. E., Walter, F. M., Rodonò, M., & Linsky, J. L. 1989, A&A, 215, 79
Pettersen, B. R. 1983, in Activity in Red Dwarf Stars, ed. P. B. Byrne & M. Rodonò (Dordrecht: Reidel), 17
Sandlin, G. D., Bartoe, J.-D. F., Brueckner, G. E., Tousey, R., & Van Hoosier, M. E. 1986, ApJS, 61, 801
Shoub, E. C. 1983, ApJ, 266, 339
Simon, T., Linsky, J. L., & Stencel, R. E. 1982, ApJ, 257, 225
Strassmeier, K. G., & Fekel, F. C. 1990, A&A, 230, 389
Summers, H. P. 1974, MNRAS, 169, 663
Swank, J. H., White, N. E., Holt, S. S., & Becker, R. H. 1981, ApJ, 246, 208
Vilhu, O. 1987, in Cool Stars, Stellar Systems, and the Sun, ed. J. L. Linsky & R. E. Stencel (Berlin: Springer), 110
Vladilo, G., Molaro, P., Crivellari, L., Foing, B. H., Beckerman, J. E., & Genova, R. 1987, A&A, 185, 233
Wahlgren, G. M., Leckrone, Leckrone, D. S., Shore, S. N., Lindler, D. J., Gilliland, R. L., & Ebbets, D. C. 1991, ApJ, 377, L41
Wahlstrøm, C. 1992, M. S. thesis, Univ. Oslo
Wahlstrøm, C., & Carlsson, M. 1994, ApJ, 433, 417
Wilson, O. C., & Bappu, M. K. V. 1957, ApJ, 125, 661
Wood, B. E., & Ayres, T. R. 1995, ApJ, in press
Zirin, H. 1975, ApJ, 199, L63